*Journal of Engineering Mathematics* **39:** 131–170, 2001.


# Generation of water waves and bores by impulsive bottom flux

M. LANDRINI and P. A. TYVAND[1]
*INSEAN, The Italian Ship Model Basin, Via di Vallerano 139, 00128 Roma, Italy*
[1]*Department of Agricultural Engineering, Agricultural University of Norway Box 5065, N-1432 Aas, Norway*

Received 28 December 1999; accepted in revised form 6 September 2000

**Abstract.** The inviscid free-surface flow due to an impulsive bottom flux on constant depth is investigated analytically and numerically. The following classes of two-dimensional flow are considered: an upwelling flow which is uniform over a half-plane, a line source/sink, and a dipole aligned along the bottom. The bottom flux is turned on impulsively and may decay with time. The fully nonlinear problem is solved numerically. A small-time asymptotic expansion to third order is found for the nonlinear problem. An asymptotic large-time solution is found for the linearized problem. A steady source will generate a pair of symmetric bores, and their breaking is investigated. A steady sink generates a depression wave if it is weak, and dip instability if it is strong. Wave breaking will occur for intermediate sink strengths. A decaying source emits solitary waves.

**Key words:** nonlinear free-surface flows, small-time expansion, boundary-integral equations, impulsive flows, water waves, bores.

## 1. Introduction

The classical Cauchy-Poisson problem is the linearized free-surface evolution from a prescribed initial elevation and initial velocity at the surface. The basic theory is found in Lamb [1]. For a finite depth we refer to Wehausen and Laitone [2, Section 22], and Whitham [3, Chapter 13]. In the present work we are concerned with the nonlinear Cauchy-Poisson problem due to initial disturbances at a fluid bottom, where an impulsive motion starts suddenly at time zero. Mei [4, Chapter 2] expounded the linear theory of transient free-surface flow due to bottom disturbances, with the application to tsunami modeling. In [5], Hammack discussed tsunami generation and the importance of nonlinearity, which can usually be neglected for tsunamis generated at typical ocean depths.

Tsunamis usually originate from rapid normal deflections at the sea-bottom. The inviscid model is appropriate for tsunami generation because of the small viscous diffusion length for the time scales involved. The flow is assumed incompressible, which means that acoustic phenomena are neglected. Their time scale is of the order of one second or shorter. From Kelvin's theorem it follows that such inviscid incompressible flows started from rest will remain irrotational through their evolution.

Practical tsunami modeling often involves bottom motions that have a horizontal length scale of the order of the fluid depth or larger. This suggests a shallow-water type of theory, although being inadequate during the impulsive start where full potential theory is needed. Vertical accelerations are important for an impulsive flow. If they are neglected, the horizontal length scale for the free-surface flow will be incorrect. However, if the bottom motion varies slowly over a wide horizontal domain, the hydrostatic description of upwelling/downwelling

will lead to quantitatively small errors. Hydrostatic theory thus requires small horizontal gradients in the normal velocity at the bottom.

The far-field due to bottom disturbances with short length scale is dominated by singularities. A source contribution is important if the net mass inflow is significant. If the net mass inflow is negligible, the far-field is usually dominated by a horizontal dipole, oriented along the bottom. A strong dipole field will result from a moving mass along the bottom (landslide), and also from a mass-conserving geological fault.

In the present paper we will consider two-dimensional flows forced by a concentrated disturbance at a uniform bottom. The forcing bottom flux, originated by singularities, is impulsively started with a possible subsequent decay.

In our general investigation of surface evolution due to bottom disturbances, we will concentrate on four themes: (I) Impulsive upwelling, which is uniform over a finite or semi-infinite length. This problem introduces itself as a key problem for developing our analytical solution procedure. From a physical point of view, it is interesting to see the nonlinearities evolving at the edge of a uniformly upwelling layer. However, the phenomenon of vortex shedding disturbs the physical realism of the present upwelling model; (II) Bottom sources and dipoles that are turned on impulsively and remain steady afterwards. The source model is not representative for tsunamis, but for a different class of flows: a steady source started from rest defines a basic class of undular bores, where the nonlinear wave front evolves slowly in time as it progresses. Breaking of the bores is also an important issue (see *e.g.* [6, 7]); (III) Bottom sinks that are turned on impulsively and remain steady. This leads to the dip formation phenomenon, which is a gravitational collapse of the free surface into the sink. Previous work has been concerned with dip formation criteria for submerged sinks. In two dimensions this has been investigated analytically and numerically by Tyvand [8] and Kim [9], respectively. The impulsive start of a submerged point sink in three dimensions has been studied analytically and experimentally by Miloh and Tyvand [10] and numerically by Xue and Yue [11]; (IV) The model relevant for tsunami generation, which involves bottom singularities that decay with time. We will concentrate on the nonlinear regime of such flows, and the transient generation of solitons and trains of oscillatory waves.

Our study of potential flows due to impulsively started singularities aims to give an understanding of the basic mechanisms in the fully nonlinear free-surface evolution. The scope of our nonlinear analysis is broader than tsunami modeling, where linear or weakly nonlinear theory is often sufficient. Our work can be regarded as a study of the nonlinear Cauchy-Poisson problem for finite depth in two dimensions. Compared with the classical starting point of initially given surface deflection and surface flow, we take a more causal starting point when the flow is solely due to bottom motion. The issues of energy and momentum transfer to the fluid are outside the scope of the classical Cauchy-Poisson problem, where the initial energy and momentum are given *a priori*.

## 2. An introductory problem: the free-surface evolution at the edge of an impulsively upwelling fluid layer

We consider an inviscid fluid layer of constant depth $h^\star$ which is at rest at negative times $t^\star < 0$. The gravitational acceleration is $g^\star$. We will consider a two-dimensional flow with surface elevation $\eta^\star(x^\star, t^\star)$ above the undisturbed level $y^\star = 0$. The $x^\star$ axis is horizontal. For positive $x^\star$ an impulsive upwelling flow is started at time zero. It is given mathematically as

a forced upwelling velocity $V_+^\star$ through the lower boundary $y^\star = -h^\star$. For negative $x^\star$ there is a forced downwelling velocity $-V_-^\star$. The unit vectors **i**, **j** correspond to the $x^\star$ and $y^\star$ axes. The important dimensionless parameter is the Froude number defined by

$$F = \frac{W^\star}{\sqrt{g^\star h^\star}} \ , \tag{1}$$

where we have introduced the velocity $W^\star = V_+^\star + V_-^\star$. We will introduce dimensionless (unstarred) quantities by using the initial fluid depth $h^\star$ as the unit of length and $W^\star$ as the unit of velocity. Consistently we introduce units of time $h^\star/W^\star$ and pressure $\rho^\star W^{\star 2}$, $\rho^\star$ being the fluid density.

The inviscid flow is governed by Laplace's equation

$$\nabla^2 \Phi = 0 \tag{2}$$

for the dimensionless velocity potential $\Phi$. The kinematic and dynamic free-surface conditions are:

$$\frac{\partial \eta}{\partial t} + \nabla\Phi \cdot \nabla\eta = \frac{\partial \Phi}{\partial y} \ , \qquad \frac{\partial \Phi}{\partial t} + \frac{1}{2}|\nabla\Phi|^2 + \frac{1}{F^2}\eta = 0 \qquad \text{on } y = \eta(x,t) \ , \tag{3}$$

respectively. As initial conditions we take an impulsive start from a situation at rest with an undisturbed free surface:

$$\eta(x,0) = 0 \qquad \Phi(x,0,0) = 0 \ . \tag{4}$$

The dimensionless upwelling and downwelling velocities for positive and negative $x$ will be denoted by $V_+$ and $-V_-$, respectively. So the impulsive forced flow is given by:

$$\frac{\partial \Phi}{\partial y} = \begin{cases} V_+ & x > 0 \\ -V_- & x < 0 \end{cases} \qquad \text{on } y = -1, \ t > 0 \tag{5}$$

and, with our definition of velocity unit, $V_+ + V_- = 1$.

In principle, the discontinuity of the velocity due to the bottom boundary condition implies a shear layer which is not presently modeled. Because of this lack of a fully reliable physical model, the following analysis should be regarded primarily as an example of the small-time expansion procedure. The Fourier expansion here is a necessary basis for the solutions below for a source and a dipole. It should be noted that the forced velocity at y=0 is not purely vertical. There is in fact a singularity in the horizontal velocity at the edge of the upwelling region. However, this bottom singularity does not give any free-surface singularity.

There is one special case which is fully consistent physically: the case of pure downwelling ($V_+ = 0$, $V_- = 1$). But this process has a short life, since the free surface is swallowed into the bottom already at $t = 1$ for $x < 0$. If the Froude number is greater than one, the third-order analysis should be good for most of this lifetime.

### 2.1. THE SMALL-TIME EXPANSION

We solve our nonlinear initial-boundary-value problem analytically by employing a small-time expansion (*e.g.* [12], [13]). In particular, we postulate:

$$(\Phi, \eta) = H(t)[(\Phi_0, 0) + t(\Phi_1, \eta_1) + t^2(\Phi_2, \eta_2) + ..] \qquad -\infty < t < \infty\ , \tag{6}$$

where the Heaviside unit step function has been introduced:

$$H(t) = 0, \quad t \leq 0 \qquad \text{and} \qquad H(t) = 1, \quad t > 0. \tag{7}$$

The governing equation and the conditions implied by the small-time expansion are:

$$\nabla^2 \Phi_n = 0 \qquad -1 < y < 0 \tag{8}$$

$$\frac{\partial\, \Phi_0}{\partial\, y} = \begin{cases} V_+ & x > 0 \\ -V_- & x < 0 \end{cases} \qquad \frac{\partial\, \Phi_n}{\partial\, y} = 0 \quad n = 1, 2, \ldots \qquad \text{on } y = -1\ . \tag{9}$$

The dynamic and kinematic conditions on the free-surface $y = 0$ are:

$$\Phi_0 = 0, \qquad \Phi_1 = -\frac{1}{2}\eta_1^2, \qquad \Phi_2 = -\eta_1(2\eta_2 + \frac{1}{2F^2}), \tag{10a}$$

$$\eta_1 = \frac{\partial\, \Phi_0}{\partial\, y}, \qquad \eta_2 = \frac{1}{2}\frac{\partial\, \Phi_1}{\partial\, y}, \qquad \eta_3 = \frac{1}{3}\frac{\partial\, \Phi_2}{\partial\, y} + \frac{1}{6}\eta_1^2\frac{\mathrm{d}^2\, \eta_1}{\mathrm{d}x^2} + \frac{1}{3}\eta_1\left|\frac{\mathrm{d}\, \eta_1}{\mathrm{d}x}\right|^2 \tag{10b}$$

### 2.2. THE FIRST-ORDER ELEVATION

The nonlinear problem will be solved most conveniently by Fourier series. For this purpose we introduce a dimensionless length $L$ of horizontal periodicity, so that the forced flow alternates between uniform upwelling and uniform downwelling for every length $L/2$ along the bottom. If $N$ is an arbitrary integer, we then consider the periodic boundary condition for the zeroth-order flow:

$$\frac{\partial\, \Phi_0}{\partial\, y} = \begin{cases} V_+ & N < x/L < N + 1/2 \\ -V_- & N - 1/2 < x/L < N \end{cases} \qquad \text{on } y = -1\ . \tag{11}$$

This is an artificial periodicity. Our original boundary-value problem is represented as the limit $L \gg 1$. The Fourier-series representation of the boundary condition (11) is then:

$$\frac{\partial\, \Phi_0}{\partial\, y} = \frac{V_+ - V_-}{2} + \frac{2}{\pi}\sum_{n\ \text{odd}} \frac{\sin(2\pi n x/L)}{n}$$

where $_{n\ \text{odd}}$ is an abbreviation for $n = 1, 3, 5, \ldots$. Therefore the first-order elevation with artificial periodicity reads:

$$\eta_1 = \frac{V_+ - V_-}{2} + \frac{2}{\pi}\sum_{n\ \text{odd}} \operatorname{sech}(2\pi n/L)\frac{\sin(2\pi n x/L)}{n}\ ,$$

The corresponding exact solution can be found by integrating up the bottom source Green function for a uniform layer [14]:

$$\eta_1 = \frac{V_+ - V_-}{2} + \frac{2}{\pi}\arctan[\tanh(\pi x/4)] \ . \tag{12}$$

The exact solution is a constant plus an odd function of $x$. The constant takes case of the net upwelling mass flux, as the odd function gives zero integral from minus to plus infinity. For later convenience, upon introducing $k = 2\pi/L$ and $k_n = nk$, we rewrite the periodic solution in the form:

$$\eta_1 = \frac{V_+ - V_-}{2} + \frac{2}{\pi}\sum_{n\ \text{odd}} \operatorname{sech} k_n \frac{\sin(k_n x)}{n} \ . \tag{13}$$

### 2.3. The second-order elevation

The first-order potential at the free surface $y = 0$ is given by:

$$\Phi_1 \ = \ -\eta_1^2/2 \ = \ -\frac{(V_+ - V_-)^2}{8} - \frac{V_+ - V_-}{\pi}\sum_{n\ \text{odd}} \operatorname{sech} k_n \frac{\sin(k_n x)}{n} -$$

$$-\frac{1}{\pi^2}\sum_{m\ \text{odd}}\sum_{n\ \text{odd}} \operatorname{sech} k_m \operatorname{sech} k_n \frac{\cos(k_{n-m}x) - \cos(k_{n+m}x)}{nm} \ .$$

We integrate the above expression in the vertical direction, from the free surface up to the bottom, where the condition of zero flux is also applied. Eventually, we obtain the potential $\Phi_1(x, y)$ everywhere in the fluid domain and, by taking the normal gradient at the free surface, the second-order wave profile reads

$$\eta_2(x) = \eta_{2\ \text{odd}} + \eta_{2\,\text{even}} \ ,$$

where

$$\eta_{2\ \text{odd}} = \frac{k}{2\pi}(V_- - V_+)\sum_{n\ \text{odd}} \operatorname{sech} k_n \tanh k_n \sin(k_n x)$$

and

$$\eta_{2\,\text{even}} = -\frac{k}{2\pi^2}\sum_{n\ \text{odd}}\sum_{m\ \text{odd}}[\ \left(\frac{1}{m} - \frac{1}{n}\right)\tanh k_{n-m}\cos(k_{n-m}x)$$

$$-\left(\frac{1}{m} + \frac{1}{n}\right)\tanh k_{n+m}\cos(k_{n+m}x)]\operatorname{sech} k_n \operatorname{sech} k_m \ .$$

### 2.4. THE THIRD-ORDER ELEVATION

The second-order potential will be written as the sum $\Phi_2 = \hat{\Phi}_2 + \Phi_2^F$, the terms $\hat{\Phi}_2$ and $\Phi_2^F$ being independent and dependent on gravity, respectively. The superscript $^F$ means Froude-number dependent. The surface elevation is decomposed in a similar way: $\eta_3 = \hat{\eta}_3 + \eta_3^F + \eta_{3\,\mathrm{lower}}$. The first two terms are the third-order elevations due to the second-order potential,

$$\hat{\eta}_3 = \frac{1}{3}\frac{\partial\,\hat{\Phi}_2}{\partial\,y}\ , \qquad \eta_3^F = \frac{1}{3}\frac{\partial\,\Phi_2^F}{\partial\,y}\ , \qquad\qquad y = 0\ ,$$

independent of and dependent on gravity, respectively. The last term (subscript: $_{\mathrm{lower}}$) is composed from lower-order contributions

$$\eta_{3\,\mathrm{lower}} = \frac{1}{6}\,\eta_1^2\,\frac{\mathrm{d}^2\eta_1}{\mathrm{d}x^2}\ +\ \frac{1}{3}\,\eta_1\,\left(\frac{\mathrm{d}\eta_1}{\mathrm{d}x}\right)^2$$

and can be simplified to:

$$\eta_{3\,\mathrm{lower}} = \frac{1}{6}\ \eta_1\ \left(\frac{\mathrm{d}\eta_1}{\mathrm{d}x}\right)^2\,\left(2 - \pi\eta_1\sinh\left(\frac{\pi}{2}x\right)\right)\ .$$

The second-order potential independent of gravity is given by the first term in third-order boundary condition (10a):

$$\hat{\Phi}_2 = -2\eta_1\eta_2\ .$$

It determines $\hat{\eta}_3$, which is a basic contribution to the third-order elevation, as it takes care of the second level in the hierarchy of nonlinear free-surface interactions.

For a pure upwelling, *i.e.* $V_+ = 1$, $V_- = 0$, the gravity-dependent elevation is found from $3F^2\eta_3^F = 2\eta_{2\ \mathrm{odd}}$ in the form

$$\eta_3^F = -\frac{k}{3\pi F^2}\sum_{n\ \mathrm{odd}}\mathrm{sech}\,k_n\tanh k_n\sin(k_n x)\ .$$

In the present theory, rather than in the potential, say, $\phi$ in the $x$-$y$ plane, we are interested in surface elevation at each order which, in turn, is given through normal derivatives $\partial\phi/\partial y$ on $y = 0$. For this purpose, solving Laplace's equation and applying the non-permeable condition at the bottom and the Dirichlet condition $\phi(x,0) = a_n\sin(k_n x - \alpha)$ at the free surface we obtain the formula $\partial\phi/\partial y = k_n\tanh k_n\ \phi(x,0)$ for the normal derivative on $y = 0$. Therefore, the normal derivative operator on each Fourier component can be replaced by a simple multiplication operator: $\partial/\partial y \quad\longrightarrow\quad k_n\tanh k_n$.

The most difficult term to evaluate in the third-order elevation is given by the second-order potential independent of gravity: $\hat{\Phi}_2 = -2\eta_1\eta_{2\,\mathrm{odd}} - 2\eta_1\eta_{2\,\mathrm{even}}$. These two inhomogeneities

are given by the Fourier series:

$$-2\eta_1\eta_{2\,\mathrm{odd}} = \sum_{n\ \mathrm{odd}} A_n \sin(k_n x) + \sum_{n\ \mathrm{odd}} \sum_{m\ \mathrm{odd}} B_{nm}(\cos k_{n-m}x - \cos k_{n+m}x) ,$$

$$-2\eta_1\eta_{2\,\mathrm{even}} = \sum_{n\ \mathrm{odd}} \sum_{m\ \mathrm{odd}} C_{nm}\cos k_{n-m}x - D_{nm}\cos k_{n+m}x +$$

$$+ \sum_{q\ \mathrm{odd}} \sum_{n\ \mathrm{odd}} \sum_{m\ \mathrm{odd}} E_{qnm}(\sin k_{n-m+q}x - \sin k_{n-m-q}x) -$$

$$- G_{qnm}(\sin k_{n+m+q}x - \sin k_{n+m-q}x)$$

We have here introduced the Fourier coefficients:

$$A_n = (V_+ - V_-)^2 \frac{k}{2\pi} \tanh k_n \operatorname{sech} k_n ,$$

$$B_{nm} = 2(V_+ - V_-)\frac{k}{2\pi^2 n} \tanh k_m \operatorname{sech} k_n \operatorname{sech} k_m ,$$

$$C_{nm} = (V_+ - V_-)\frac{k}{2\pi^2}\left(\frac{1}{m} - \frac{1}{n}\right) \tanh k_{n-m} \operatorname{sech} k_n \operatorname{sech} k_m ,$$

$$D_{nm} = (V_+ - V_-)\frac{k}{2\pi^2}\left(\frac{1}{m} + \frac{1}{n}\right) \tanh k_{n+m} \operatorname{sech} k_n \operatorname{sech} k_m ,$$

$$E_{qnm} = \frac{k}{\pi^3 q}\left(\frac{1}{m} - \frac{1}{n}\right) \tanh k_{n-m} \operatorname{sech} k_q \operatorname{sech} k_n \operatorname{sech} k_m ,$$

$$G_{qnm} = \frac{k}{\pi^3 q}\left(\frac{1}{m} + \frac{1}{n}\right) \tanh k_{n+m} \operatorname{sech} k_q \operatorname{sech} k_n \operatorname{sech} k_m .$$

The matrices D and G are very similar to C and E, respectively, the change of sign in the n-terms being the only difference. However, this gives no simplification, because we sum over positive values only, $n = 1, 3, 5, \ldots$

The corresponding third-order elevation is given by:

$$
\begin{aligned}
3\hat{\eta}_3 \;=\; & k \sum_{n \text{ odd}} A_n \tanh k_n \, \sin k_n x + \\
& + k \sum_{n \text{ odd}} \sum_{m \text{ odd}} (n-m)(B_{nm} + C_{nm}) \tanh k_{n-m} \, \cos k_{n-m} x - \\
& - k \sum_{n \text{ odd}} \sum_{m \text{ odd}} (n+m)(B_{nm} + D_{nm}) \tanh k_{n+m} \, \cos k_{n+m} x + \\
& + k \sum_{q \text{ odd}} \sum_{n \text{ odd}} \sum_{m \text{ odd}} E_{qnm} [(n-m+q) \tanh k_{n-m+q} \, \sin k_{n-m+q} x - \\
& \qquad - (n-m-q) \tanh k_{n-m-q} \, \sin k_{n-m-q} x \, ] \\
& - k \sum_{q \text{ odd}} \sum_{n \text{ odd}} \sum_{m \text{ odd}} G_{qnm} [(n+m+q) \tanh k_{n+m+q} \, \sin k_{n+m+q} x - \\
& \qquad - (n+m-q) \tanh k_{n+m-q} \, \sin k_{n+m-q} x \, ] \, .
\end{aligned}
\tag{14}
$$

## 3. Impulsive waves due to a source at a uniform bottom

We now return to our original problem where a forced impulsive flow is started at time zero. Let us first consider the case of a source with initial volume flux $Q^\star$, given per unit length perpendicular to the flow. It is concentrated at the point $x^\star = 0$, either as an upward flow (bottom source) or downward flow (bottom sink). The Froude number is now defined as

$$
F = \frac{Q^\star}{\sqrt{g^\star h^{\star\,3}}} \tag{15}
$$

and an appropriate choice of the unit velocity is $Q^\star / h^\star$. As in the previous sections, the unit of length is the initial fluid depth $h^\star$ and, consistently, $h^{\star\,2}/Q^\star$ and $\rho^\star (Q^\star/h^\star)^2$ are the dimensionless time and pressure units. The bottom source is assumed to decay exponentially in time as $Q^\star \mathrm{e}^{-\sigma^\star t^\star}$. The dimensionless decay rate is defined as:

$$
\sigma = \sigma^\star h^{\star\,2} / Q^\star \, . \tag{16}
$$

So the dimensionless source strength is $\mathrm{e}^{-\sigma t}$. The total dimensionless volume (per length of the source) being emitted by the source during its lifespan is given by $\sigma^{-1}$. It is of interest to keep this dimensionless area constant and vary the Froude number.

Regardless of whether a bottom source or dipole (*cf.* Appendix A) is considered, the governing equations are the same as in Section 2, except for the bottom boundary condition, which now reads:

$$
\frac{\partial \Phi}{\partial y} = \mathrm{e}^{-\sigma t} \, \delta(x) \qquad\qquad y = -1, \;\; t > 0 \, , \tag{17}
$$

where $\delta(x)$ denotes the Dirac delta function.

Following the procedure sketched in the previous section, through the small time expansion (6), we now recast the fully nonlinear problem in the form of a set of problems for the Laplace equation (8) with free-surface boundary conditions (10a), (10b). As the bottom-boundary condition (17) suggests, the potential to each order is written as the sum of a regular potential $\varphi_n$ and a singular potential $\psi_n$:

$$\Phi_n = \varphi_n + \psi_n \ . \tag{18}$$

We first consider the singular potential given by the source at the bottom with the zero-potential condition at $y = 0$.

The complex version of the unexpanded singular potential is:

$$\Psi = \frac{1}{2\pi} \mathrm{e}^{-\sigma t} \log \frac{\sinh\left(\frac{\pi}{2} z\right) + \mathrm{i}}{\sinh\left(\frac{\pi}{2} z\right) - \mathrm{i}} \ .$$

Here the complex variable $z = x + \mathrm{i}y$ is introduced. This formula has been derived from the Schwarz-Christoffel confomal mapping for a semi-infinite horizontal layer, which was given in [14]. The normal derivative at the free surface is found to be:

$$\left.\frac{\partial \psi}{\partial y}\right|_{y=0} = -\Im\mathfrak{m}\left(\frac{\mathrm{d}\Psi}{\mathrm{d}z}\right)\bigg|_{y=0} = \frac{1}{2}\,\mathrm{e}^{-\sigma t}\,\mathrm{sech}\left(\frac{\pi}{2} x\right) \ .$$

The same formula for the surface flow can be derived by the image method. But this method has the disadvantage that the series for the potential does not converge.

The bottom conditions for the regular potentials are:

$$\frac{\partial \varphi_n}{\partial y} = 0 \ , \qquad y = -1 \tag{19}$$

for $n = 1, 2, ...$

### 3.1. First-order elevation

The first-order elevation is given by the normal derivative of the singular potential:

$$\eta_1 = \frac{1}{2}\,\mathrm{sech}\left(\frac{\pi}{2} x\right) \ . \tag{20}$$

We note the simple result for the surface elevation just above the source: $\eta_1(0) = 1/2$. In the case of a submerged line source [8] this first-order elevation just above the source is $1/\pi$.

The boundary-value problems will be solved most conveniently by Fourier series. For this purpose we introduce a dimensionless length $L$ of horizontal periodicity. This means that we assume the following boundary condition along the bottom:

$$\frac{\partial \psi}{\partial y} = \mathrm{e}^{-\sigma t} \sum_{n=-\infty}^{+\infty} (-1)^n \ \delta\left(x - n\frac{L}{2}\right) \ , \qquad y = -1, \ t > 0 \ . \tag{21}$$

A Fourier expansion for this boundary condition, which generates the zeroth-order potential by an array of singularities, does not exist. But the potential itself exists, in terms of generalized functions. Its first-order elevation can be found by taking the $x$-derivative from the upwelling problem investigated by in Section 2. The result is:

$$\eta_1 = \frac{4}{L} \sum_{\text{n odd}} \operatorname{sech}\left(\frac{2\pi n}{L}\right) \cos\left(\frac{2\pi n}{L} x\right) \ , \tag{22}$$

where n-odd is an abbreviation for $n = 1, 3, 5, \ldots$. In the following, we use the compact notation:

$$k = \frac{2\pi}{L} \qquad k_n = nk \ ; \tag{23}$$

therefore $k_n$ denotes the $n$-th harmonic wavenumber. The first-order elevation with artificial periodicity is then:

$$\eta_1 = \frac{2}{\pi} k \sum_{\text{n odd}} \operatorname{sech} k_n \, \cos k_n x \ . \tag{24}$$

As discussed in the previous section, a shortcut to solve the periodic boundary-value problems below is using $\partial/\partial y \to k_n \tanh k_n$, for each Fourier component, to obtain the normal derivative of the potential on $y = 0$ starting from the free-surface potential.

In equivalence with taking the artificial length $L$ to be much greater than one, we have now introduced the lowest-harmonic wave number $k$ as our artificial parameter to be much smaller than one. Its higher harmonics are $k_n$ . We will evaluate the series (24) by truncating it after a number $n_{\max}$. Asymptotically, as $L \gg 1$ (or $k \ll 1$), the approximate solution (24) converges to the exact solution (20).

The relationship between the present problem and the impulsive upwelling problem of Section 2 is intriguing. Although Equation (24) is a Fourier-series solution of our bottom-source problem with a spatial period $L$, we could find it only indirectly through the upwelling problem. The obtained solution is a Fourier-series solution valid for the free-surface flow generated by an array of bottom sources and sinks, in spite of the fact that it could not be found by Fourier expanding our bottom condition.

These formulas for the first-order elevation represent a bottom source. The same expressions with opposite sign will be valid for a bottom sink.

### 3.2. Second-order elevation

The regular first-order potential at the free surface $y = 0$ is given by:

$$\varphi_1 \ = \ -\frac{1}{2}\,\eta_1^2 \ = \ -\frac{1}{8} \operatorname{sech}^2\left(\frac{\pi}{2} x\right) \ , \tag{25}$$

which can be recast as a Fourier series with a wave number $k$:

$$\varphi_1 = -\left(\frac{k}{\pi}\right)^2 \sum_{\text{n odd}} \sum_{\text{m odd}} \operatorname{sech} k_n \operatorname{sech} k_m \, \left[\cos(k_{n-m} x) + \cos(k_{n+m} x)\right] \tag{26}$$

We integrate the Fourier series and apply the condition of impermeability at the bottom. For the purpose of higher-order analysis we give the second-order elevation by the formula:

$$\begin{aligned} 2\eta_2 \;=\; & -\left(\frac{k}{\pi}\right)^2 \sum_{\text{n odd}} \sum_{\text{m odd}} \operatorname{sech} k_n \operatorname{sech} k_m \;\times \\ & \times \left[\, k_{n-m} \tanh k_{n-m} \cos(k_{n-m}x) + k_{n+m} \tanh k_{n+m} \cos(k_{n+m}x) \,\right] \\ & - 2\sigma \frac{k}{\pi} \sum_{\text{n odd}} \operatorname{sech} k_n \cos k_n x \;. \end{aligned} \tag{27}$$

As a last term in Equation (27) we have included the second-order contribution from the decaying source potential. If we introduce its exact instead of periodic version, we have the second-order elevation:

$$\begin{aligned} \eta_2 \;=\; & -\frac{1}{2}\left(\frac{k}{\pi}\right)^2 \sum_{\text{n odd}} \sum_{\text{m odd}} \operatorname{sech} k_n \operatorname{sech} k_m \;\times \\ & \times \left[\, k_{n-m} \tanh k_{n-m} \cos(k_{n-m}x) + k_{n+m} \tanh k_{n+m} \cos(k_{n+m}x) \,\right] \\ & - \sigma \frac{1}{4} \operatorname{sech} (\frac{\pi}{2}x) \;. \end{aligned} \tag{28}$$

### 3.3. THIRD-ORDER ELEVATION

The regular second-order potential at the free surface $y = 0$ is:

$$\begin{aligned} \varphi_2 \;=\; & (\frac{k}{\pi})^3 \sum_{\text{n odd}} \sum_{\text{m odd}} \sum_{\text{q odd}} \operatorname{sech} k_n \operatorname{sech} k_m \operatorname{sech} k_q \;\times \\ & \times \left\{ k_{n-m} \tanh k_{n-m} [\cos(k_{n-m-q}x) + \cos(k_{n-m+q}x)] + \right. \\ & \left. + k_{n+m} \tanh k_{n+m} [\cos(k_{n+m-q}x) + \cos(k_{n+m+q}x)] \;\right\} \\ & + 2\sigma \left(\frac{k}{\pi}\right)^2 \sum_{\text{n odd}} \sum_{\text{m odd}} \operatorname{sech} k_n \operatorname{sech} k_m [\cos(k_{n-m}x) + \cos(k_{n+m}x)] \\ & - \frac{1}{F^2} \frac{k}{\pi} \sum_{\text{n odd}} \operatorname{sech} k_n \cos k_n x \;. \end{aligned} \tag{29}$$

The total surface elevation is given by:

$$\eta_3 = \underbrace{\frac{1}{3} \frac{\partial \Phi_2}{\partial y}}_{\eta_{3,\infty} + \eta_{3,F}} + \underbrace{\frac{1}{6}\eta_1^2 \frac{\mathrm{d}^2 \eta_1}{\mathrm{d}x^2} + \frac{1}{3}\eta_1 \left|\frac{\mathrm{d}\eta_1}{\mathrm{d}x}\right|^2}_{\eta_{3\eta_1}} , \tag{30}$$

where (*cf.* third part of Equation (10a)) the first term is split in a zero-gravity contribution and a truly Froude-number dependent term. The second and last contribution are grouped into $\eta_{3\eta_1}$,

the nonlinear contribution coming directly from $\eta_1$. Here we will apply the exact formulas for the first-order elevation. We also have to add the contribution from the singular potential. The final result is then:

$$\begin{aligned}
\eta_3 \;=\; & \frac{1}{3}\left(\frac{k}{\pi}\right)^3 \sum_{\text{n odd}} \sum_{\text{m odd}} \sum_{\text{q odd}} \operatorname{sech} k_n \operatorname{sech} k_m \operatorname{sech} k_q \;\times \\
& \times \{k_{n-m} \tanh k_{n-m} \,[\; k_{n-m-q} \tanh k_{n-m-q} \cos(k_{n-m-q}x) + \\
& \qquad + k_{n-m+q} \tanh k_{n-m+q} \cos(k_{n-m+q}x)] + \\
& + k_{n+m} \tanh k_{n+m} [\; k_{n+m-q} \tanh k_{n+m-q} \cos(k_{n+m-q}x) \\
& \qquad + k_{n+m+q} \tanh k_{n+m+q} \cos(k_{n+m+q}x)] \,\} \\
& + \frac{2}{3}\sigma \left(\frac{k}{\pi}\right)^2 \sum_{\text{n odd}} \sum_{\text{m odd}} \operatorname{sech} k_n \operatorname{sech} k_m \;\times \\
& \times [k_{n-m} \tanh k_{n-m} \cos(k_{n-m}x) + k_{n+m} \tanh k_{n+m} \cos(k_{n+m}x)] - \\
& - \frac{1}{3F^2} \frac{k}{\pi} \sum_{\text{n odd}} k_n \operatorname{sech} k_n \tanh k_n \cos k_n x \;+\; \frac{\pi^2}{384} \operatorname{sech}^5\left(\frac{\pi}{2}x\right) [\, 3\cosh(\pi x) - 5\,] + \\
& + \frac{\sigma^2}{12} \operatorname{sech}\left(\frac{\pi}{2}x\right) \;.
\end{aligned} \tag{31}$$

Here we have avoided the artificial periodicity wherever an exact formula is available.

## 4. Numerical solution of the exact problem

The evolution of the flow on a longer time-scale is studied by solving numerically the fully nonlinear problem. Here we briefly sketch the adopted algorithm, more details are provided by Tyvand and Landrini in [15] and in the references cited there and below. We solve an initial value problem for the Euler equations:

$$\nabla \cdot \boldsymbol{u} \;=\; 0 \;, \qquad \frac{\mathrm{D}\,\boldsymbol{u}}{\mathrm{D}\,t} \;=\; -\frac{1}{\rho}\nabla p + \boldsymbol{g} \;, \tag{32}$$

where $\boldsymbol{u}$ is the fluid velocity, with the no–penetration condition $\boldsymbol{u} \cdot \boldsymbol{\nu} \;=\; \mathrm{e}^{-\sigma t}\delta(\boldsymbol{P}_S)$ on the bottom and, respectively, the kinematic and dynamic boundary conditions:

$$\frac{\partial\, \boldsymbol{P}(\xi, t)}{\partial\, t} \;=\; \boldsymbol{u} \qquad \frac{\partial\, u_\xi(\xi, t)}{\partial\, t} \;=\; \frac{\partial}{\partial\, \xi}\left(\frac{1}{2}u_\xi^2 - gy\right) \tag{33}$$

on the free surface $\mathcal{F}$. Equations (33) are a Lagrangian description of the free surface $\boldsymbol{P}[x(\xi, t), y(\xi, t)]$, where $\xi$ is a Lagrangian parameter and $u_\xi$ is the covariant component of $\boldsymbol{u}|_{\mathcal{F}}$ along the tangential vector $\partial\boldsymbol{P}/\partial\xi$. This allows to follow large deformations up to possible incipient wave breaking.

The unsteady fully nonlinear problem is numerically solved through a boundary-integral approach coupled with a time marching procedure (a standard fourth-order Runge–Kutta

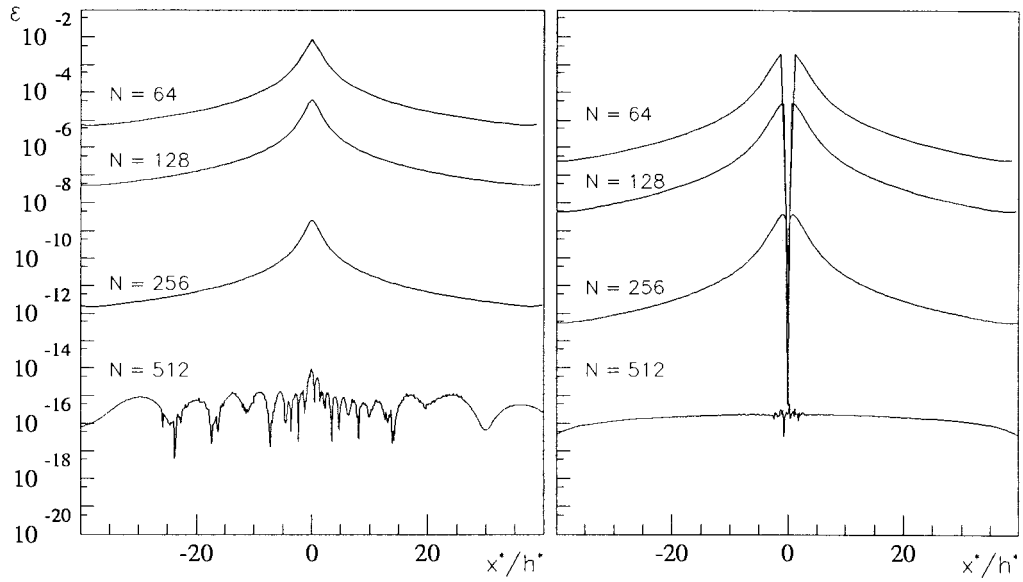


*Figure 1.* Solution by integral equation. Absolute error ε in determining $\partial\Phi_0/\partial y$ on $y = 0$ for increasing number $N$ of unknowns. Left hand plot: velocity induced by a source (*cf.* Equation 20). Right hand plot: velocity induced by a dipole (*cf.* Equation A4).

scheme). Starting from the Poincaré formula discussed by Bassanini *et al.* in [16], we may express the velocity field by

$$\boldsymbol{u}(\boldsymbol{Q}) \;=\; \nabla_Q \int_{\mathcal{F}} \boldsymbol{u}\cdot\boldsymbol{\nu}\,\hat{G}\mathrm{d}S_P \;+\; \nabla_Q \times \int_{\mathcal{F}} \boldsymbol{u}\times\boldsymbol{\nu}\,\hat{G}\mathrm{d}S_P \;+\; \boldsymbol{u}_S(\boldsymbol{Q})\;, \tag{34}$$

*i.e.* 'directly' in terms of the normal $\boldsymbol{u}\cdot\boldsymbol{\nu}$ and tangential $\boldsymbol{u}\times\boldsymbol{\nu}$ velocity components on $\mathcal{F}$. The singular part of the velocity field due to source, dipole or combination of singularities is explicitly given by $\boldsymbol{u}_S(\boldsymbol{Q})$. The presence of the bottom boundary is accounted for through the kernel $\hat{G}$, obtained by modification of the two-dimensional fundamental solution $\log|\boldsymbol{P}-\boldsymbol{Q}|$ for Laplace equation according to the method of images.

At a given instant of time, we assume that $u_\xi$ is known and the unknown velocity component $\boldsymbol{u}\cdot\boldsymbol{\nu}|_{\mathcal{F}}$ is evaluated through the integral equation following from (34) when $\boldsymbol{P}\in\mathcal{F}$ and taking the normal projection. Once the velocity field on $\mathcal{F}$ is evaluated, the solution can be prolonged in time by the free-surface evolution equations (33). Eventually, new geometry and boundary data are obtained and the procedure can be re–initialized.

The contour integrals are discretized by the Euler–McLaurin summation formula which, in combination with trigonometric polynomials, allows for high accuracy (see [17] for a rigorous analysis). The iteration technique developed in [18] is adopted for solving the linear algebraic system. For longer simulations and large number $N$ of unknowns, multipole expansion and fast summation techniques (described in [19]) have been applied to speed up the solution procedure. A typical test of convergence under grid refinement is given in Figure 1, where the error in evaluating $\boldsymbol{u}\cdot\boldsymbol{\nu}\equiv\partial\Phi_0/\partial y$ on the free surface is shown for increasing number $N$ of Lagrangian points on the free surface.

Sawtooth instabilities, first reported by Longuet-Higgins and Cokelet in [20], are removed by a high-order filter [21].

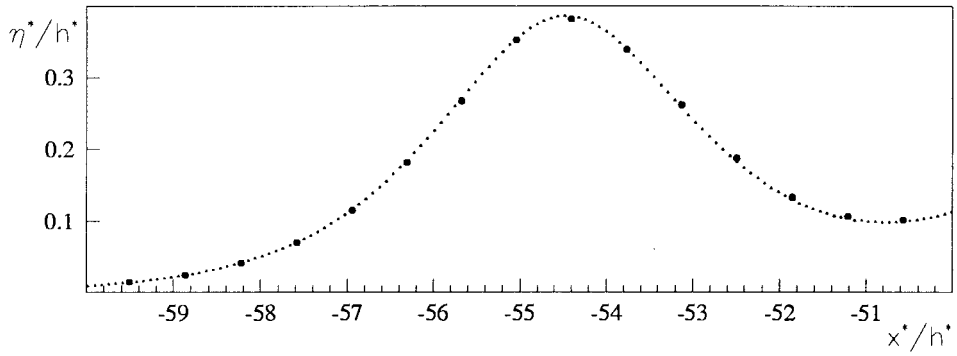


*Figure 2.* Convergence test under grid and time-step refinement. Comparison of the leading wave of an undular bore ($F = 0{\cdot}5$, $\sigma = 0$ and $t^\star/T_{\rm lw} = 50$) obtained by the coarsest (large symbols) and the finest (tiny symbols) discretization from Table 4.

During the simulation, for time long enough, the distribution of Lagrangian markers above a submerged source tends to be highly non-uniform. This can cause loss of accuracy and a strongly localized unstable motion of the free surface. We have removed the problem by redistributing periodically the free-surface points around the singularity using a cubic spline based algorithm. This can degrade the overall accuracy up to third-order in mesh-spacing, though the main effect is expected to be around the singularity. To the same purpose, an alternative grid-control procedure has been also developed and tested. In particular, new free-surface particles are inserted as soon as the spacing between the original markers becomes too large. The location and the tangential velocity of the new particles are initialized by cubic fitting. The results obtained by using the two different procuderes are essentially the same, thus confirming each other. The high resolution needed by sink-generated flows has been achieved by the use of tanh-grading for the initial distribution of markers around $x = 0$.

We have checked all the computations shown in the main text by halving both the initial spacing $\delta\ell^\star/h^\star$ of the Lagrangian markers and the time step $\Delta t^\star/T_{\rm lw}$ until an acceptable convergence is achieved. As a typical example, the Table 4 reports the height $\eta_0^\star/h^\star$ above a constant source, $F = 0{\cdot}5$, for $t^\star/T_{\rm lw} = 50$ and for increasingly refined discretization. The two

*Table 1.* Convergence test under refinement of discretization. Effect of main discretization parameters on the wave height $\eta_0^\star/h^\star$ over a constant source, $F = 0{\cdot}5$, for $t^\star/T_{\rm lw} = 50$.

| $\delta\ell^\star/h^\star$ $\Delta t^\star/T_{\rm lw}$ | 0·64 1/10 | 0·32 1/20 | 0·16 1/40 | 0·08 1/80 |
|---|---|---|---|---|
| $\eta_0^\star/h^\star$ | 0·2388911736952251 | 0·2371882781916181 | 0·2371157325963261 | 0·2371139364995115 |

most refined solutions differ by less than 0·0008 %. Less easy to compare are differences in wave height for those markers largely drifted by the flow. In Figure 2 we simply superimpose the coarsest grid and the most refined (symbols represent the Lagrangian markers) and this gives an idea of the satisfactory convergence achieved. If superimposed, results by the two most refined discretizations would be undistinguishable.

We also recall that, in the numerical simulation, a truncated free surface has to be considered. Therefore, for each case discussed, we ruled out the effect of the finite horizontal extent of the free surface by doubling it, keeping constant $\Delta t$ and $\delta\ell$, and verifying the invariance of

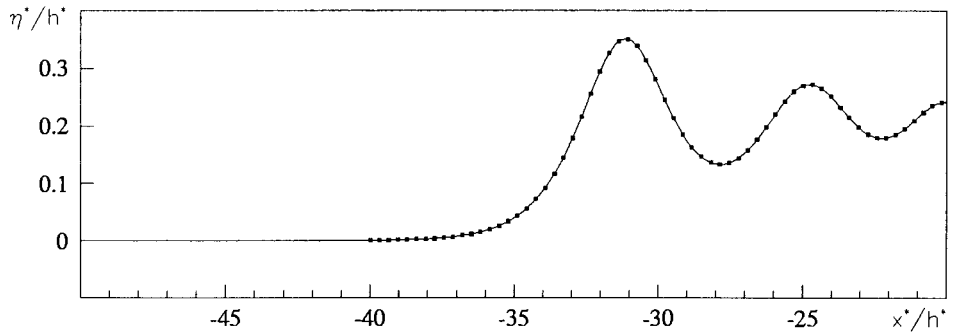


*Figure 3.* Effect of horizontal truncation of the computational domain. Comparison of the leading wave of an undular bore ($F = 0{\cdot}5$, $\sigma = 0$ and $t^\star/T_{\mathrm{lw}} = 60$) for $L_{\max}/h^\star = -40$ (symbols) and $L_{\max}/h^\star = -80$ (solid line).

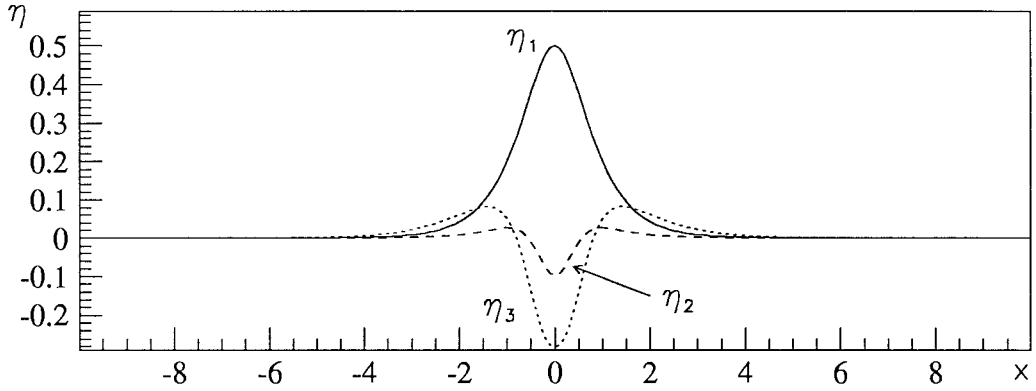


*Figure 4.* Shapes of $\eta_1$, $\eta_2$, $\eta_3$ for $F = 0{\cdot}5$ and $\sigma = 0$. All variables are non-dimensional. In the series $L = 100$, $n_{\max} = m_{\max} = q_{\max} = 200$. Non-dimensional variables according to the text.

the solution. Actually, Figure 3 shows that, even when the leading wave is close to the edge of the computational domain, the solution are practically the same.

Typically, at the end of the simulations, the error in mass conservation is below 0·001%, while the imbalance between the integrated input of power due to the singularity and the energy in the fluid system is at most of order 1%.

## 5. Discussion

### 5.1. Range of validity of the small-time expansion

Figure 4 shows the height functions $\eta_1$, $\eta_2$ and $\eta_3$ for a constant source, $\sigma = 0$, with strength $F = 0{\cdot}5$. It can be seen that, for this choice of the parameters, higher-order contributions act to reduce the central hump and spreading the disturbance over a larger horizontal extent. This behaviour is not entirely due to the gravity, which actually enters the problem only at third order. Even at this order, a more subtle balance of different tendencies can be observed through Figure 5 where $\eta_3$ is split according to Equation (30). Both $\eta_{3\eta_1}$ (pumped by the first-order solution) and $\eta_{3,F}$ (directly related to the gravity) act qualitatively as $\eta_2$, with a larger spreading action for the Froude-dependent term. The zero-gravity term gives a larger and narrower positive peak with smaller depression around it.

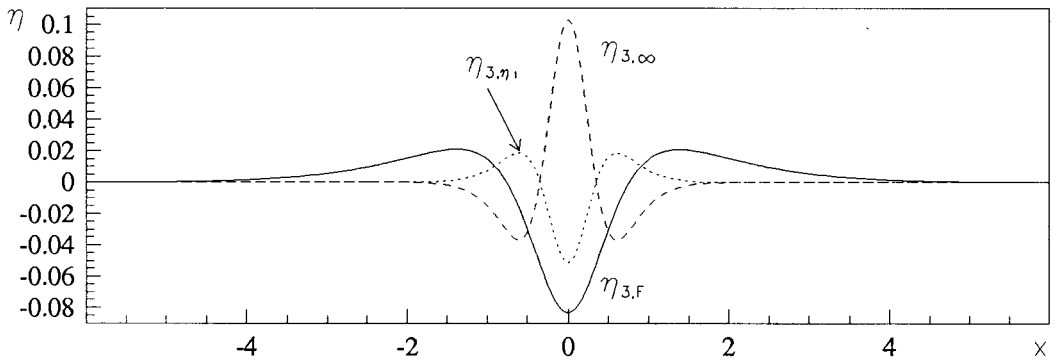


*Figure 5.* Terms forming $\eta_3$ (*cf.* Equation (30)) for $\sigma = 0$. The Froude-dependent term $\eta_{3,F}$ is shown for $F = 1$. Non-dimensional variables according to the text.

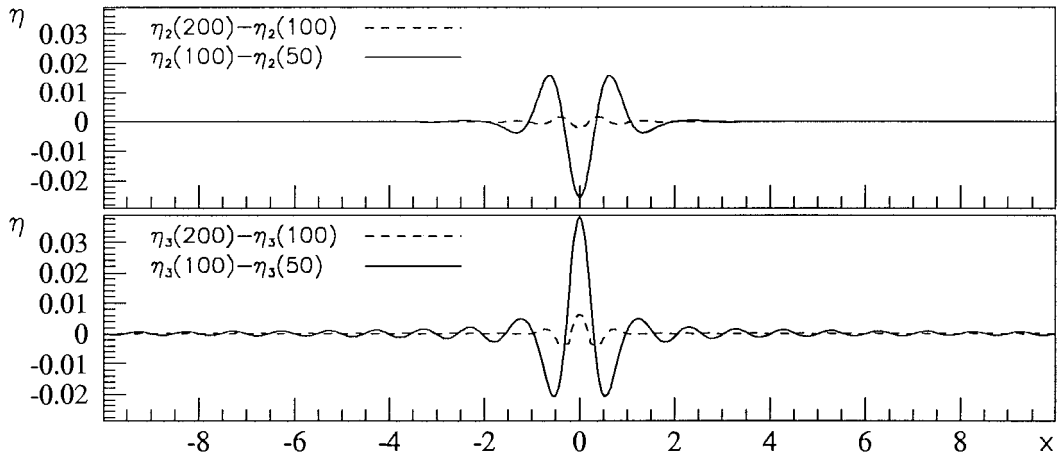


*Figure 6.* Convergence of series expansion for $\eta_2$ (top) and $\eta_3$ (bottom). Same of Figure 4. Differences are plotted between the sums obtained by using $n_{\max} = m_{\max} = q_{\max} = 50$, 100 and 200; the same $L = 100$ is adopted. Non-dimensional variables according to the text.

Series entering in Equations (28) and (31) for $\eta_2$ and $\eta_3$, respectively, cannot be summed up in closed form, and the effect of truncation of the Fourier series is of concern. This is considered in Figure 6 for the same case as above, where the point-wise difference of $\eta_2$ and $\eta_3$ as obtained by doubling the highest modes $n_{\max} = m_{\max} = q_{\max}$ is plotted against the horizontal coordinate $x$. Computations have been performed using quadruple precision, without special means to improve the speed of convergence of the series which turned out to be quite slow, with larger variations concentrated around the origin. By further doubling the truncation limits of summations, we detected no changes graphically.

After the heuristic convergence-check of our boundary-integral equation solver by comparing with the analytical solution for $\Phi_0$ (*cf.* Figure 1), we have solved numerically also the velocity fields $\nabla\Phi_n$, $n = 1, 2$, and the same results for $\eta_1$, $\eta_2$ and $\eta_3$ have been obtained with larger efficiency.

The range of validity of our small-time expansion is discussed by comparing the semi-analytical wave profiles with those obtained by solving numerically the fully nonlinear problem. In Figure 7 the two solutions are shown for a given source strength, $F = 1$, and increasing values of the decaying factor $\sigma$. For $\sigma \leq 0{\cdot}5$, the small-time expansion (dashed lines) agrees

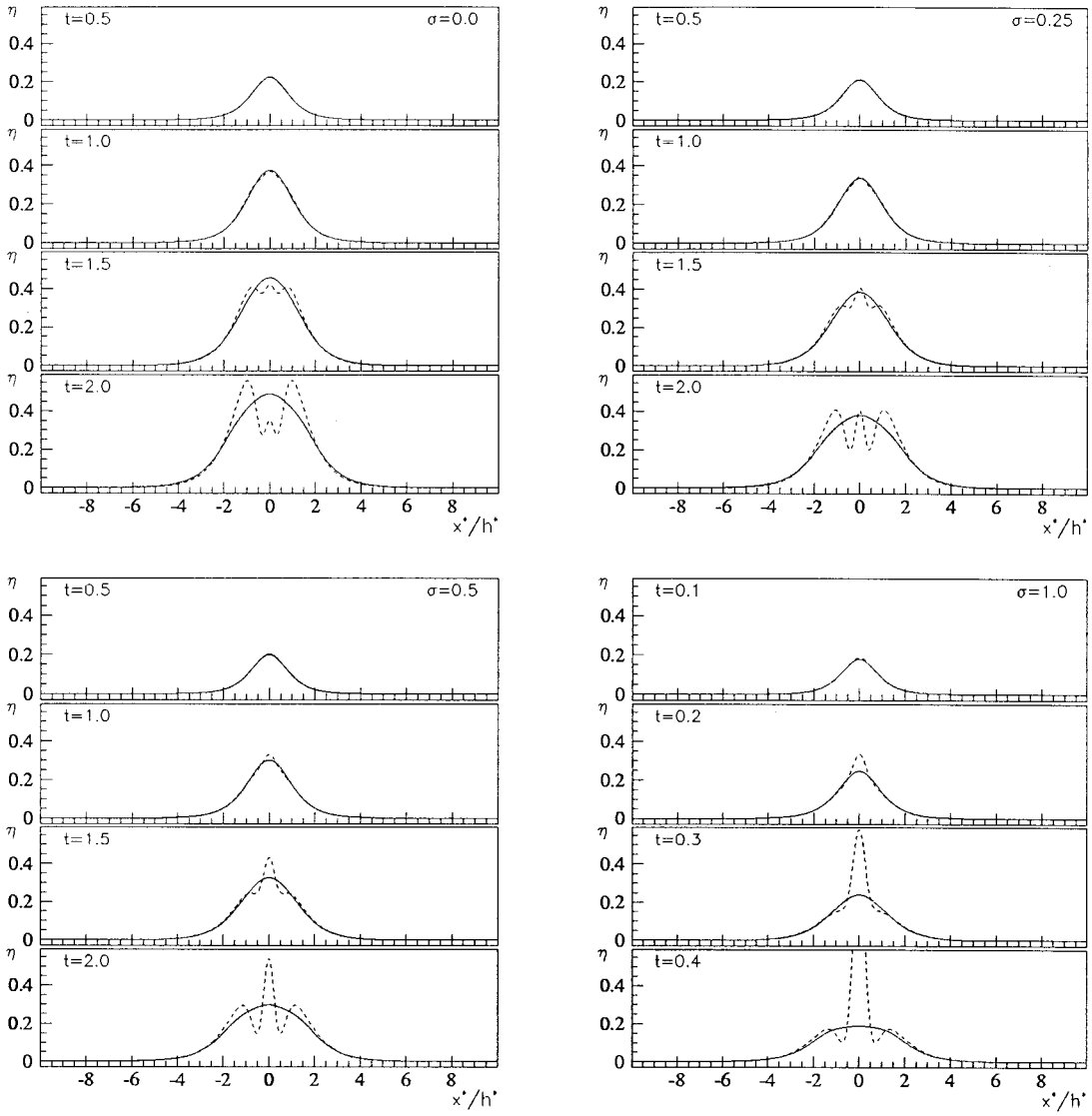


*Figure 7.* Comparison between the small-time expansion to third order (dashed lines) and the fully nonlinear (numerical) solution for $F = 1{\cdot}0$, $\sigma = 0, 0{\cdot}25, 0{\cdot}5, 1$. Non-dimensional time $t = t^{\star}Q^{\star}/h^{\star 2}$.

well with the fully nonlinear solution (solid lines) up to $t \sim \mathcal{O}(1)$. Within this time scale, the behaviour simply consists in the smooth growth of the water level just above the source: a symmetric hump is formed and, after reaching a maximum level, starts to increase its horizontal extent. As can be expected, for non-zero $\sigma$ the vertical growth is smaller while the horizontal spreading is comparable for all the $\sigma$ considered.

In all the considered cases, for larger time, the small-time expansion deviates from the nonlinear solution. For $\sigma = 0$, the central hump decreases and two lateral peaks emerge with a separation distance (slightly) increasing in time. For finite $\sigma$, the lateral humps still appear, but the central peak remains higher and progressively overestimates the fully nonlinear solution. This trend is magnified in the case $\sigma = 1$ (bottom-right plot), where the exponential behaviour

is soon poorly approximated by the Taylor expansion and prevents the semi-analytical solution to agree with the nonlinear one beyond $t \sim \mathcal{O}(0{\cdot}1)$.

### 5.2. LONG-TIME BEHAVIOUR FOR $\sigma = 0$

On the basis of our semi-analytical solution, the initial free-surface evolution can be generally drawn as a process during which the mass injected by the source accumulates in the form of a hump above the initial free surface level. In the following sections we investigate the free-surface evolution on a time-scale beyond the limit of applicability of our small-time expansion analysis. To the purpose, we will mainly rely on the numerical solution of the exact (inviscid) problem, as obtained by the method described in Section 4. Occasionally, we solved also the linearized version of the problem.

Figure 8 provides a first description of the flow for a constant source, $\sigma = 0$, and (relatively) small Froude number, $F = 0{\cdot}25$. The fully nonlinear solution shows how gravity reacts to restore the initial level, resulting in a (weak) decrease of the central peak accompanied by the emission of waves symmetrically propagating outwards. The phenomenon is now dominated by gravity and a more appropriate time-scale is provided by the speed of long waves, $c^\star_{\rm lw} = \sqrt{g^\star h^\star}$, and a suitable time unit results as $T_{\rm lw} = h^\star/c^\star = \sqrt{h^\star/g^\star}$. A pair of undular bores emerge, symmetrically propagating outwards with a velocity of order $c^\star_{\rm lw}$ and leaving beyond an almost flat free surface with a level slightly below $\eta/F \simeq 0{\cdot}5$. In the bottom plot, the six waves profiles are superimposed and the enlarged view of the free surface around the origin witnesses both the presence of a small heap of fluid, above the mean level, and the stationary character quickly reached by the free surface close to the source.

#### 5.2.1. *Asymptotic interpretation of the flow due to a steady source at small Froude number*

*Primitive considerations.* For a small Froude-number source, outward radiation of gravity waves prevents the accumulation of a high local elevation above the source. The flow is of the impulsive type only for $0 < t < F$, during which a local surface heap of order $F$ is accumulated above the source. Later on, since this amplitude is small, a wave front will develop with a propagation velocity close to $c^\star_{\rm lw}$, which reads $1/F$ in our non-dimensional variables.

Eventually, the dominating wave will be a bore of almost constant height $\eta^\star_{\rm b}$, since gravity tends to level out the surface in the bulk of the bore. Mass balance gives the relationship $2\eta^\star_{\rm b} c^\star_{\rm lw} = Q^\star$ and the dimensionless bore height then satisfies the equation

$$\eta_{\rm b} = F/2 \ . \tag{35}$$

This almost uniform bore is a shallow-water phenomenon, which establishes after the wave front has traveled several unit lengths horizontally. The bore front is wavy, but the bulk of the bore is increasingly dominated by the average elevation $F/2$. This estimate is better the smaller the Froude number is.

To confirm the simplified analysis, a set of computations for decreasing source strength have been performed and reported in Figure 9 together with the linearized solution (thick-dashed lines). The qualitative behaviour is the same for all of the considered Froude numbers, with the leading crest faster for higher Froude numbers. The enlarged view in the bottom plot clearly shows the tendency to recover the estimate (35) as $F$ decreases, with the bulge of fluid eventually disappearing for smaller and smaller $F$. Conversely, when the source strength is increased, the central bulge increases its amplitude with respect to the surrounding mean

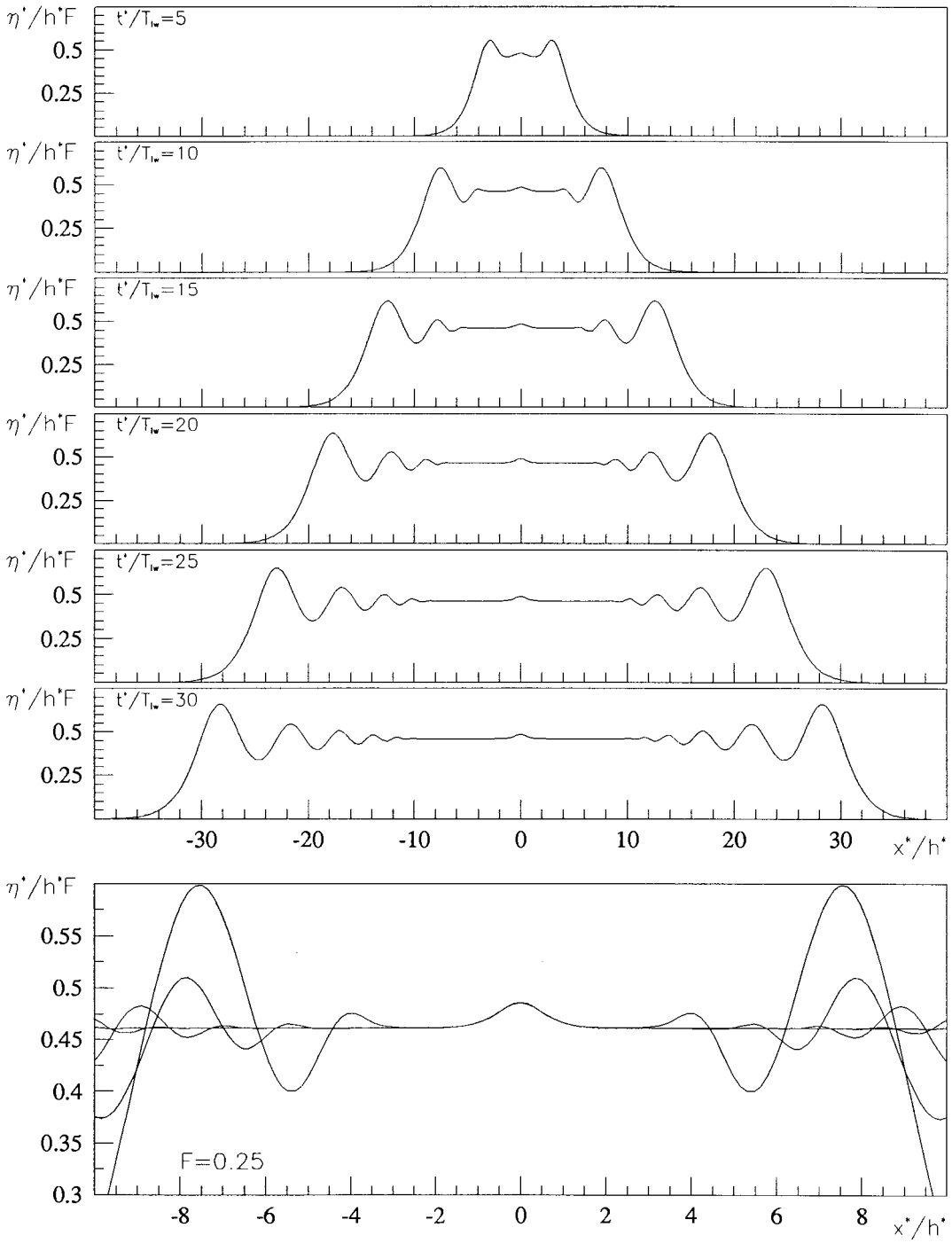


*Figure 8.* Free-surface motion due to a source of constant strength, $\sigma = 0$ (numerical solution of the fully nonlinear problem). Top: snapshots for $F = 0{\cdot}25$. Bottom: enlarged view around the origin; the same time instants as above are superimposed.

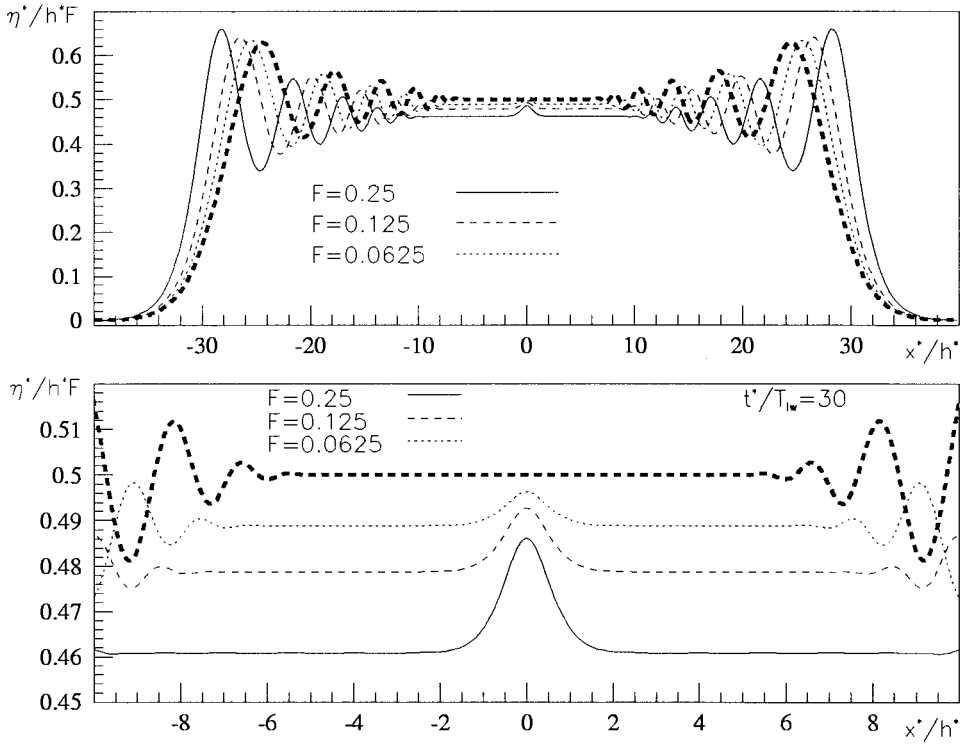


*Figure 9.* Undular bore due to a constant source, $\sigma = 0$, for decreasing strength $F$. Thicker dashed lines represent the linear solution. Top: comparison of the free surface at $t = 30$. Bottom: enlarged view around the origin.

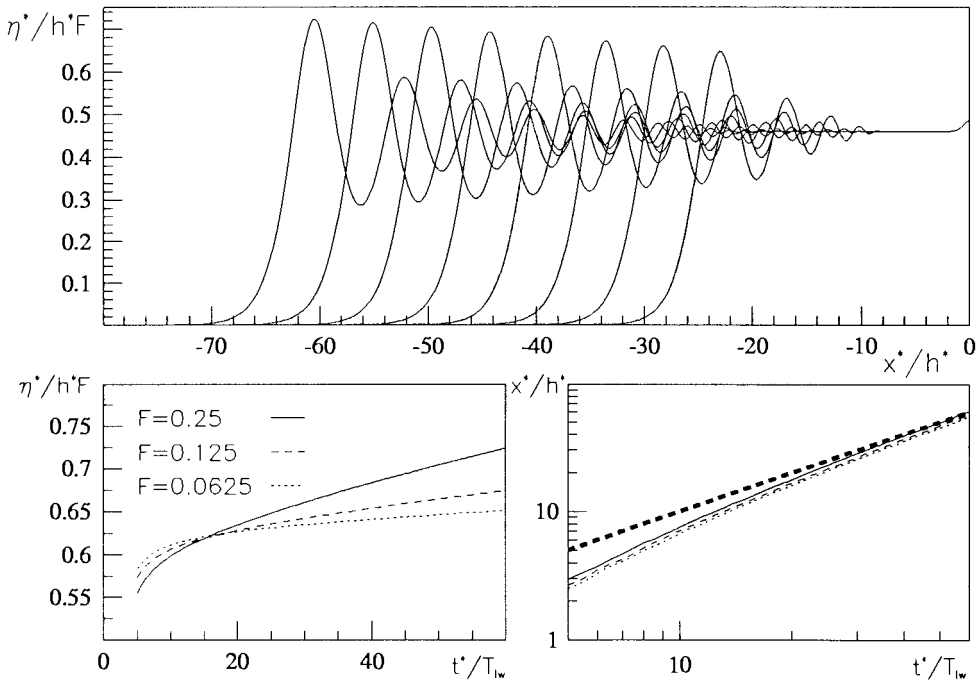


*Figure 10.* Evolution of the undular bore due to a constant source. Top plot: free surface for $F = 0{\cdot}25$ in the range $t \in [25, 60]$, $\Delta t = 5$. Bottom plots: time evolution of the leading crest of the bore (amplitude and longitudinal position) for decreasing $F$. The thicker dashed line represents $x = t$.

water level which, in turn, decreases for higher $F$. It appears, indeed, reasonable that larger bore systems are needed to drain away the greater mass of fluid injected by stronger sources.

The late evolution is discussed in Figure 10. In the top plot, for $F = 0{\cdot}25$, left-hand wave profiles in the range $t^\star/T_{\rm lw} \in [25, 60]$ are superimposed every five time-units, showing that the lengthening of the undular bore is accompanied by the growth in amplitude of the waves forming it. This behaviour is typical also for smaller source strengths. In the same figure, the two lower plots report the history of leading crests for several $F$. To analyze the numerical simulation, it is assumed that the highest Lagrangian marker represents the actual leading crest well enough. The amplitude increases with a growth rate smaller for smaller $F$ but still positive, even for $F = 0{\cdot}0625$. Finally, the diagram of the horizontal location of maxima gives a rough idea of the propagation velocity of leading crests, which results slightly larger than $c^\star_{\rm lw}$.

*Asymptotic analysis for the bore front.* Whitham, [3, p. 442], gave an asymptotic analysis for the behaviour of a wave front on constant depth due to an initial hump of fluid released from rest. For long-enough evolution, the flow is governed by the gravitational time scale and, in the following, time and velocity units are changed to $T_{\rm lw}$ and $c^\star_{\rm lw}$, respectively.

The concentrated initial elevation is assumed to have a length scale equal to the depth or smaller. It gives rise to two equal waves, one propagating to the right and one to the left. The problem is governed by Laplace's equation with linearized free-surface conditions. A release of fluid of positive elevation integrated up as unit area (volume per length) at time zero will then, after a time $t \gg 1$, give the surface elevation:

$$\eta = \frac{1}{2}\left(\frac{2}{t}\right)^{1/3} \mathrm{Ai}\left[\left(\frac{2}{t}\right)^{1/3}(|x| - t)\right] ,$$

where Ai denotes the Airy function (see [22, p. 446]). This formula is asymptotically valid for as long as $t \gg 1$, which means that the wave front must have traveled a horizontal distance much greater than the fluid depth. The positive localized elevation at $t = 0$ which gave rise to this wave, may in fact be due to an impulsive bottom source that put a unit volume into the fluid during the infinitesimal time interval from $t = 0$ to $t = 0^+$.

Now we focus the attention on a steady source impulsively turned on at $t = 0$. The dimensionless volume put into the fluid per time unit is represented by the source Froude number. The idea is to integrate in time all later contributions after the initial one that can have influenced the local motion. This constrains the admissible values of $x$: we should never go farther than a dimensionless distance $t/2$ away from the wave front located at $|x| = t$, because the asymptotic analysis breaks down. Going further into the bore further reduces the large ratio (propagation length)/(depth) which is vital for the asymptotics. This means that younger and younger wave fronts (not yet fully matured for the asymptotic analysis) are being fed into the integrated elevation. It also means that we are picking contributions from the older waves farther and farther into their oscillatory tails, which will give less accuracy.

The asymptotically integrated elevation for the linearized bore from a source is

$$\eta = \frac{1}{2}F\int_0^t \mathrm{e}^{-\sigma\tau}\left(\frac{2}{t-\tau}\right)^{1/3} \mathrm{Ai}\left[\left(\frac{2}{t-\tau}\right)^{1/3}(|x| + \tau - t)\right] \mathrm{d}\tau , \tag{36}$$

where also the effect of the decaying singularity is accounted for. The time interval of integration is the same as the time elapsed since the impulsive start. The singularity in the

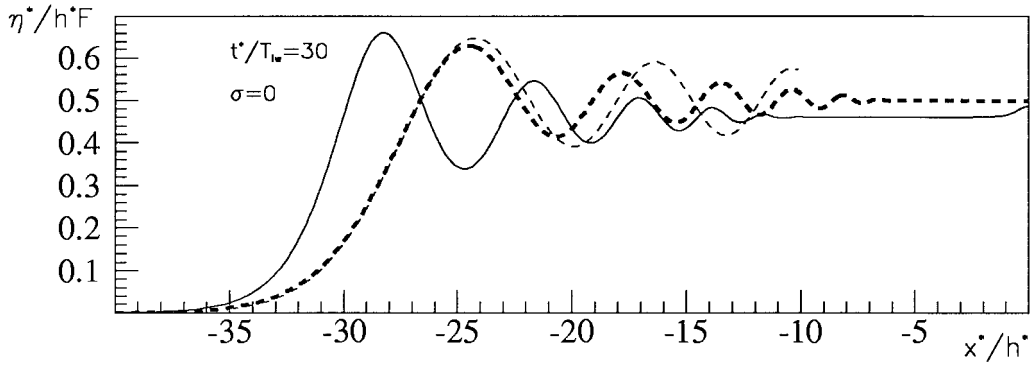


*Figure 11.* The bore front, for $F = 0{\cdot}25$, as predicted by the asymptotic formula (36) (thin-dashed line) is compared with the linear (thick-dashed line) and the nonlinear (solid line) computations.

integrand occurring as $\tau \longrightarrow t$ does not give any convergence problems. In Figure 11, for $F = 0{\cdot}25$, fully nonlinear and linear (numerical) results are compared with the asymptotic wave form of Equation (36). The asymptotic bore front nicely agrees with the linear solution, and both are slightly retarded with respect to the nonlinear wave profile, which is apparently steeper. Past the leading crest, the Airy function solution exhibits a slower spatial decay and becomes increasingly worse as we move into the bore. As was first shown in [7], inspection of Figures 9 and 11 reveals that for weaker bores the wave system is more stretched as a result of the prevailing dispersive effects. Consistently, the linear solution exhibits, for a given time, a wider distribution of waves.

*Improved bore model.* We may cope with the nonlinear behaviour of the bore front by accounting for nonlinearities from a kinematic point of view. This is done by including amplitude dispersion as given by the Korteweg-deVries equation [3, p. 463]. In the dimensionless gravitational variables, the average wave velocity in the bulk of a bore of height $\eta_b$ is:

$$c = 1 + \frac{3}{2}\eta_b \ . \tag{37}$$

From Equation (35) we estimate the wave velocity as a function of the source Froude number $F$:

$$c = 1 + \frac{3}{4}F + \mathcal{O}(F^2) \ . \tag{38}$$

This is correct to first order in a Froude-number expansion. As an example, we take $F = 0{\cdot}25$ which gives $c = 1{\cdot}19$. This nonlinear kinematic effect of amplitude dispersion explains well the forward displacement of each wave crest in Figure 9, compared with linear theory. However, the dynamical interaction between the different wave crests is not included in this kinematic argument. The numerical solution shows that nonlinear interaction makes the leading wave crest grow at the expense of the following waves, and the bore becomes more flat apart from the increased peak at the front.

A qualitative argument for the dynamical interaction between the wave crests follows from a consideration of group velocity: since the group velocity of the waves in the bulk of the bore is greater than the velocity of the wave front, it is plausible that the wave-energy is being focussed at the leading crest. The finite outward fluid flow inside a nonlinear bore also promotes wave energy transport towards the leading crest.

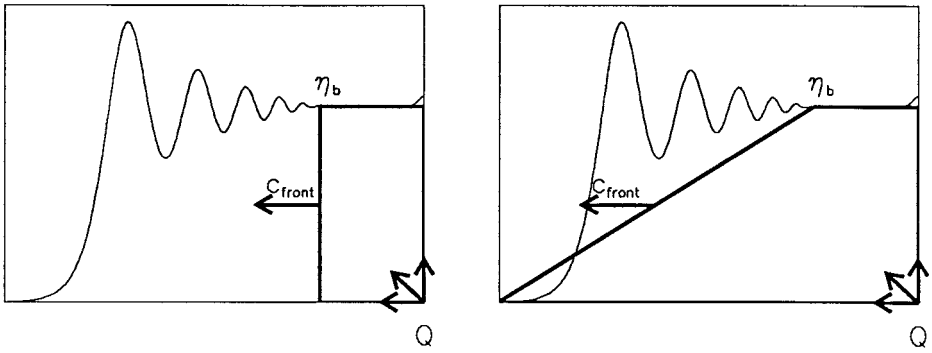


*Figure 12.* Simplified bore models. Left hand: box approximation. Right hand: trapezoid approximation.

The elementary bore model (35) is the most primitive way to account for the mass balance due to the steady source. The whole bore is imagined as a rectangular box (*cf.* Figure 12) expanding to the left and right with the exact shallow-water velocity. In reality, there is a finite slope at a non-breaking bore front, and the position of the central bore front can be defined by half the bore elevation $\eta_b/2$. The amplitude dispersion vanishes in the beginning of the front and is maximal at the first peak behind the front. The propagation velocity $c_{front}$ of the central bore front is thus given by Equation (37). Because of this, we now imagine the bore as a trapezoid and the mass balance between the source and the expanding bore front gives

$$2\eta_b\, c_{front} = F \ . \tag{39}$$

As front velocity we take the average of the shallow-water propagation velocity (unity) and the wave velocity inside the bore, $c_{front} = (c+1)/2 = 1 + (3/4)\eta_b$, which, when inserted in Equation (39), gives a quadratic equation in $\eta_b$ with the solution:

$$\eta_b = \frac{2}{3}\left(\sqrt{1+\frac{3}{2}F} - 1\right) \ . \tag{40}$$

Although it still requires a non-breaking bore, the 'trapezoid model' does not necessarily require $F \ll 1$ as the 'box approximation' above and, in fact, values for $\eta_b/F$ are in nice agreement with fully nonlinear computations:

| | $F = 1{\cdot}0$ | $F = 0{\cdot}75$ | $F = 0{\cdot}5$ | $F = 0{\cdot}25$ | $F = 0{\cdot}125$ | $F = 0{\cdot}0625$ |
|---|---|---|---|---|---|---|
| Equation (40) | 0·3874 | 0·4068 | 0·4305 | 0·4603 | 0·4785 | 0·4888 |
| Numerical simulation | 0·3904 | 0·4090 | 0·4318 | 0·4608 | 0·4786 | 0·4888 |

where in the worst case, $F = 1{\cdot}0$, we have less than 1% error. From this trapezoid estimate of the bore elevation, we find the improved estimate $c = \sqrt{1 + (3/2)F}$ for the wave velocity inside the bore and a Froude number expansion here recovers Equation (38).

5.2.2. *Larger F: the appearance of breaking*

So far, small-time expansion and asymptotic analysis offer a good qualitative understanding of the results obtained by the numerical solutions of the exact problem. We also are able to give fairly precise estimates through relatively simple formulas.

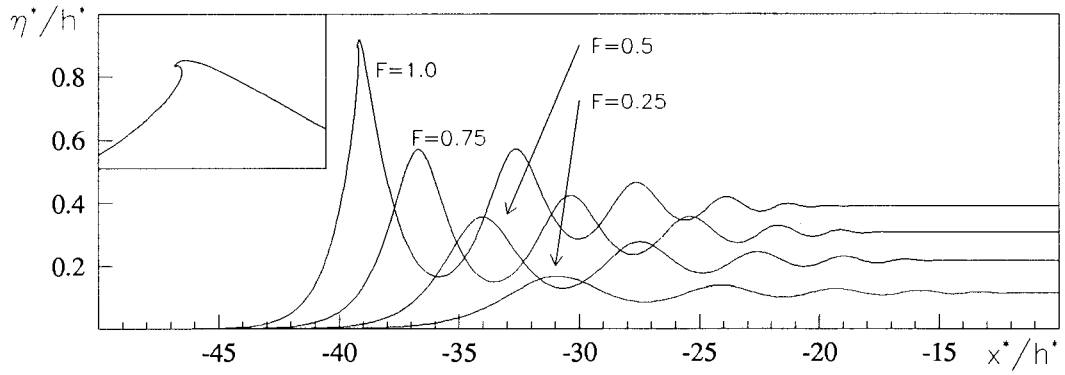


*Figure 13.* Undular bore generated by constant sources in the range $0{\cdot}25 \leq F \leq 1$. For all cases the free surface refers to $t^\star/T_{\mathrm{lw}} = 32{\cdot}5$ but for $F = 1$ where surface breaking (detailed in the top-left plot) is evidenced for $t^\star/T_{\mathrm{lw}} \simeq 32{\cdot}24$.

Further increasing the Froude number introduces a new feature: the breaking of the leading wave. The problem is numerically studied by Teles da Silva and Peregrine [7] by following the evolution of an already established jump $\Delta$ smoothly reconciled through the initial wave profile $\eta = \Delta/2(1 - \tanh(\alpha x))$. In particular, they observed three different regimes: non-breaking undular bores for $\Delta <\sim 0{\cdot}3$, undular breaking bores and breaking bores for $\Delta >\sim 0{\cdot}7$.

For the problem considered here, the first regime has been extensively analyzed in previous paragraphs. In Figure 13 wave profiles in the range $0{\cdot}25 \leq F \leq 1$ are superimposed for $t \sim 32{\cdot}5$ to show the transition from undular to undular breaking bores. As discussed, the mean level above the source increases as $\sim F^{0{\cdot}5}$, Equation (40); the leading crest is steeper the larger $F$ is and propagates faster because of amplitude dispersion. In particular, for the leading peaks shown in the figure, we have:

| | $F = 0{\cdot}25$ | $F = 0{\cdot}5$ | $F = 0{\cdot}75$ | $F = 1{\cdot}0$ |
|---|---|---|---|---|
| $\eta$ | 0·1666 | 0·3563 | 0·5706 | 0·9196 |
| $x$ | −30·9368 | −33·9954 | −36·70476 | −39·17567 |

Actually, for $F = 1$, the simulation has been stopped around $t \sim 32{\cdot}24$ because of the tiny nascent breaker shown in the top-left corner. For $F < 1$, simulations are continued on a longer time-scale. In all cases, no sign of breaking has been detected, though the amplitude of leading crests still (weakly) grows for $t \sim 200$. A similar behaviour can be observed in Teles da Silva and Peregrine results [7, Figure 3], even for the smallest $\Delta = 0{\cdot}1$ and after a quite long evolution, $t = 140$. Moreover, although we expect that the leading crest will be a solitary wave [23], Figure 10 suggests that the time needed to reach this asymptotic behaviour increases nonlinearly as $F$ increases. Finally, it is plausible that on this long time scale viscous effects could play a relevant role.

We have not tried to identify sharply the limiting source strength for the first breaking appearance. In Figure 14, we simply show the time $t_{\mathrm{br}}$ requested for the leading-wave front to become vertical as a function of the Froude number. The curve, for $F > 2$, is flattened around $t_{\mathrm{br}} \sim 5$, while, as $F$ decreases, the time for breaking increases sharply, approaching,

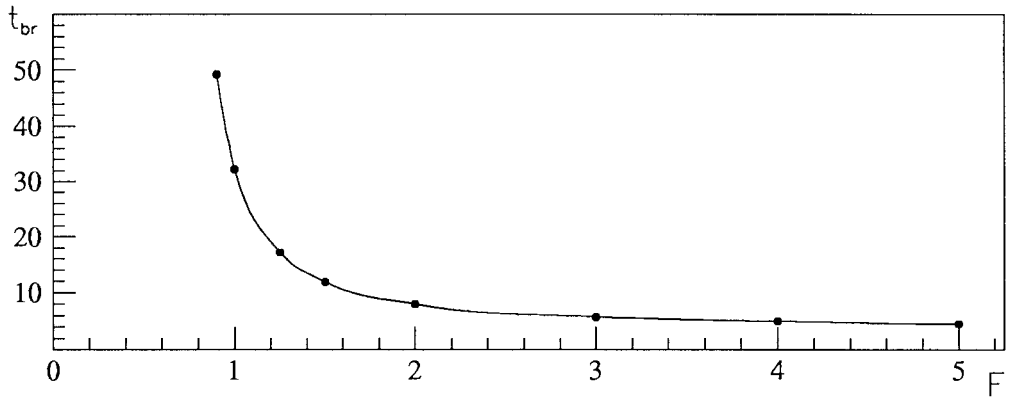


*Figure 14.* Time $t_{\rm br}$ for the leading-wave front to become vertical as a function of the Froude number. Symbols • denote actual computations.

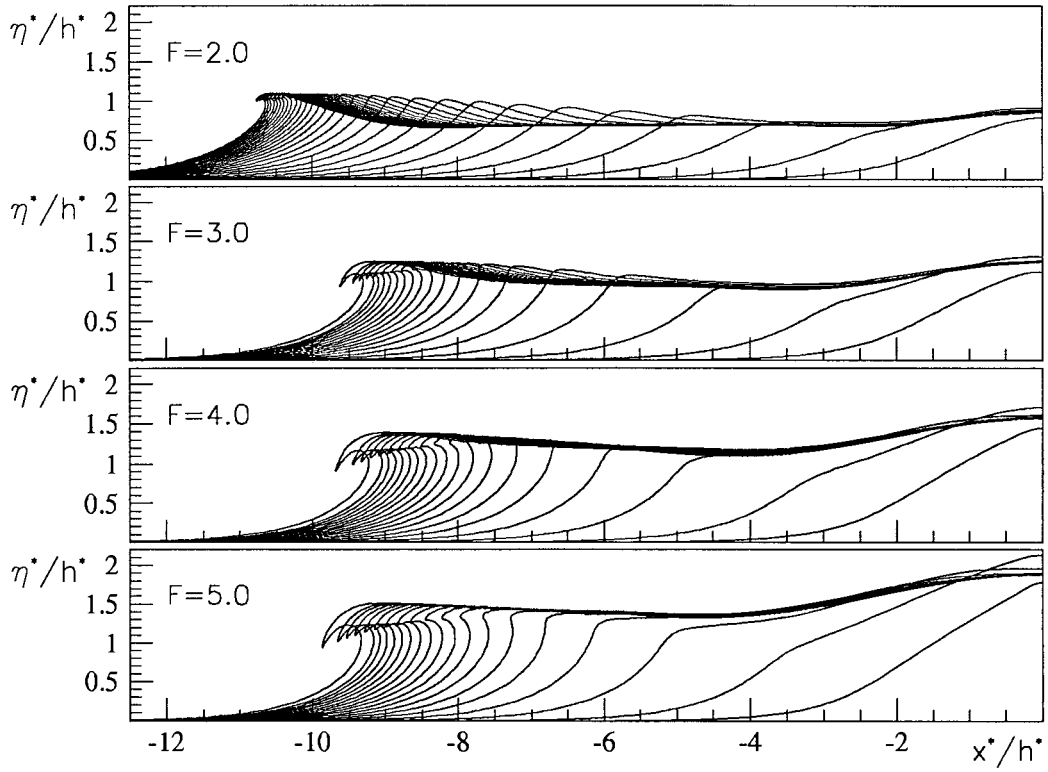


*Figure 15.* Evolution toward breaking of the bore due to a constant source, $\sigma = 0$, for increasing source strength. Last time reported: $t = 8{\cdot}53$, $7{\cdot}787$, $6{\cdot}239$ and $5{\cdot}94$ from top down, respectively.

according to our simulations, a limiting value in between $F = 0.75$ (non-breaking case) and $F = 0.9$ (breaking case).

For breaking bores in the range $F = 0{\cdot}9, \ldots, 1{\cdot}75$, several undulations are still present behind the bore front but, because wave breaking prevents to proceed further in the simulation, we cannot assess if, in the steady regime, we would observe an undular bore with a weak breaker at the leading front or the undulations would eventually disappear completely.

The plunging breaker is increasingly larger for stronger sources (*cf.* Figure 15), while the time scale needed for its appearance is progressively shorter. Interestingly, the location of the plunger is roughly the same for the cases reported in figure, although the height increases slightly. The undulations behind the bore-front have no time to develop and we enter in the regime of breaking bores with a flat free surface behind. Actually, the hump centered around $x = 0$ witnesses the presence of the submerged source and it is spread over a larger area with respect to cases with smaller $F$. At this stage the bore has entirely attained the character of breaking bore without residual undulations.

The initial conditions considered in the paper by Teles da Silva and Peregrine are quite different from the case considered here. In our problem, the flow is uniquely determined by $F$ while in the former both $\Delta$ and the imbalance between the upstream and downstream currents enter the problem. On the other hand, the source induces local effects which are fairly prominent as $F$ increases, which can hamper the study of the nascent breaker. In spite of this, our present results agree with the findings of Teles da Silva and Peregrine.

### 5.3. WAVES DUE TO A CONSTANT SINK

Waves generated by a submerged sink are now discussed through the computations reported in Figure 16 for $F = -0{\cdot}25$ and $\sigma = 0$. As the small-time expansion suggests, the motion starts as a growing depression around the sink. On a longer time scale, after reaching a minimum, the induced hollow slightly diminishes as a result of the gravity reaction and tends to attain a constant level. In the meanwhile, the horizontal extent of the depression increases as an obvious consequence of the mass-defect due to the sink. The front of this spreading depression propagates with a velocity of order $c_{\mathrm{lw}}^{\star}$ and appears as a train of waves with decreasing amplitude and wavelength when moving from the front to the location above the sink. Within a linearized theory, the solution can be obtained by simply replacing $(\eta, F)$ by $(-\eta, -F)$ which clearly justifies the appearance of a depression wave. By allowing $F$ to be negative, the asymptotic formula (36) also covers the case of a weak sink. This is actually done in Figure 17, where for $t = 30$ nonlinear, linear and (linear) asymptotic solutions are compared. As expected, linear solutions agree to the same extent as for $F > 0$ (correct front location and different spatial decaying). The nonlinear wave profile generated by a sink displays different features compared with those for $F > 0$. In particular, the location of leading crest is closer to the singularity compared with the linear solution: the opposite as for the source case. As a consequence, the nonlinear depression wave cannot be classified as a bore because nonlinearity tends to smear out the front instead of steepening it.

The wiggled system inside the depression is unexpected on the ground both of the linear analysis and of the corresponding nonlinear results for a source with $F = 0{\cdot}25$ (*cf.* Figure 8). This feature strikingly appears when we compare nonlinear solutions in Figures 9 and 18. The nonlinear phenomenon of amplitude dispersion offers an explanation: the oscillating wiggles are fed locally by the sink (or the source) and propagate outwards. In a bore, $F > 0$, such short waves travel faster than the bore-front due to amplitude dispersion ($c_{\mathrm{b}} > c_{\mathrm{front}}$) and tend to merge with the leading peak. Eventually they disappear, leaving a waveless region inside the nonlinear bore. For $F < 0$, the front moves faster and the local oscillations in the depression are maintained and fed by the sink.

A closer look at Figures 16–18 reveals that there is a steady positive deflection of the surface inside the depression, just above the sink. It is identical to the positive heap in the surface elevation above a source. The reason that this heap also exists above a sink, is that

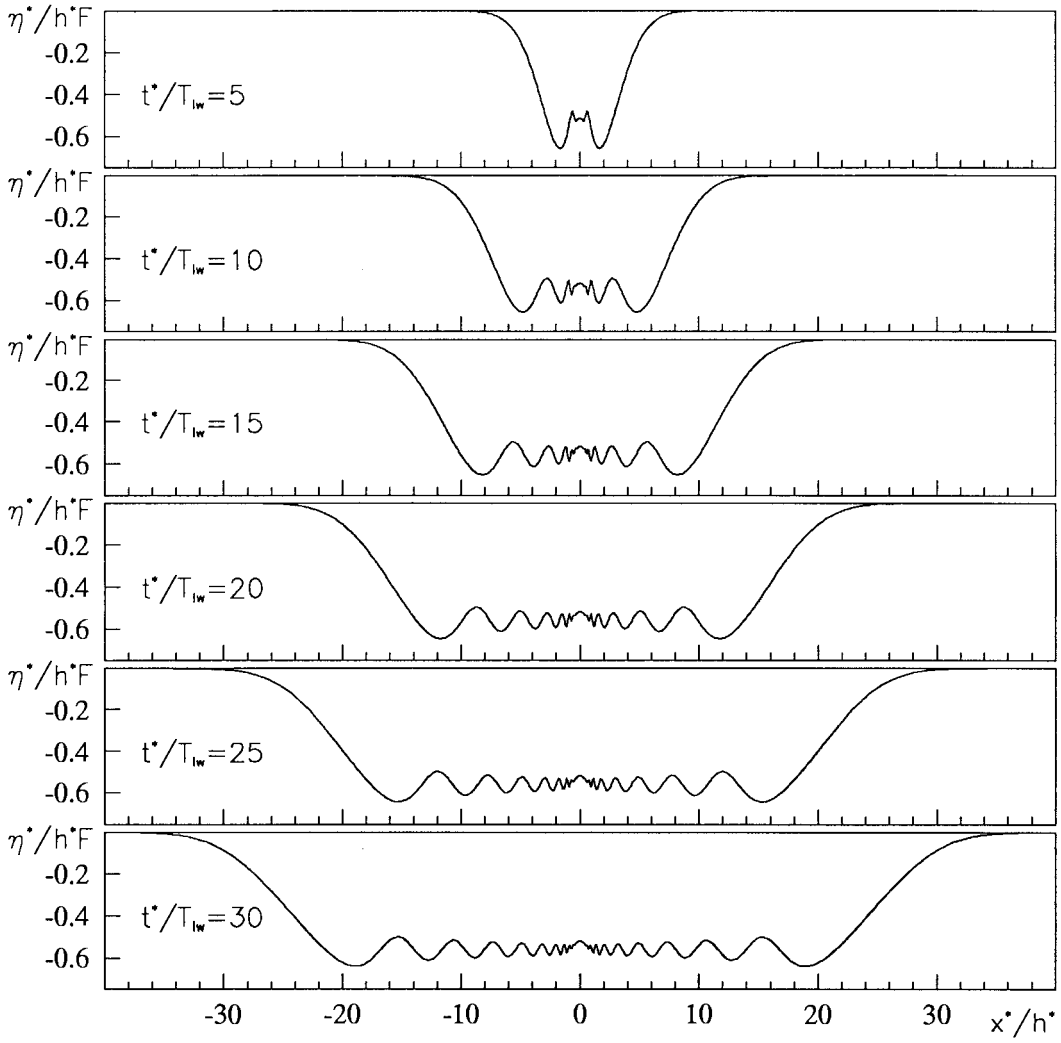


*Figure 16.* Free-surface motion due to a constant sink ($F = -0{\cdot}25$, $\sigma = 0$).

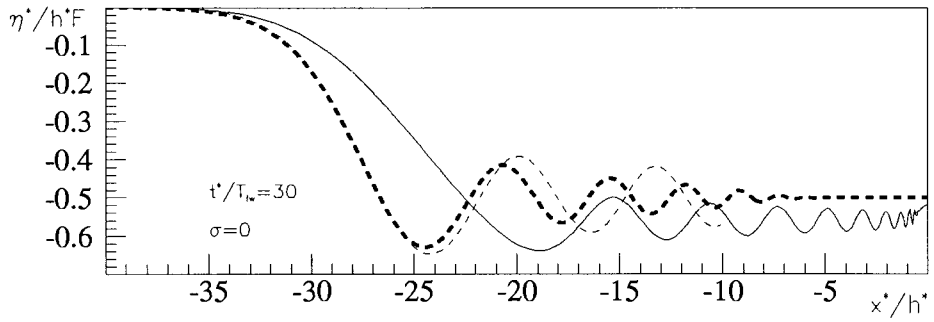


*Figure 17.* Free-surface motion due to a constant sink ($F = -0{\cdot}25$, $\sigma = 0$). Comparison of asymptotic prediction (thin dashed line), linear (thick dashed line) and nonlinear computations (solid line).

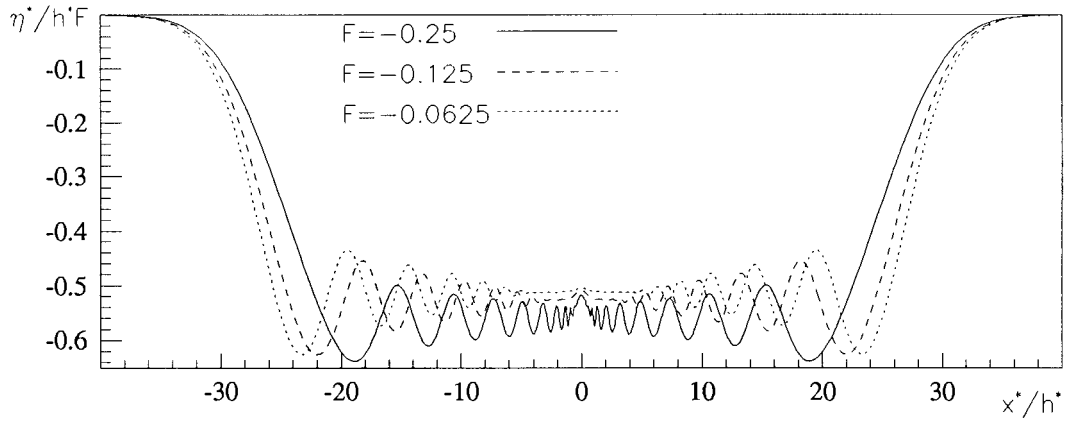


*Figure 18.* Free-surface motion due to a constant sink ($\sigma = 0$). Comparison of the free surface at $t^\star/T_{\rm lw} = 30$ for decreasing $F$.

steady nonlinear free-surface flows are reversible in time (such lack of distinction between steady flows induced by sources or sinks is observed by Koerber and Forbes in [24]). When we compare nonlinear sink flows with corresponding source flows, it is necessary to redefine the Froude number. The effective Froude number for a steady source/sink flow is:

$$F_{\rm eff} = F\,(1+\eta_{\rm b})^{-3/2}\ .$$

This redefinition is needed because there exists no undisturbed fluid level in the steady problem. There is a flat surface at infinity, serving as reference level for steady flow. But it corresponds to the bore level of the transient flow, not the undisturbed level. A good approximation for $\eta_{\rm b}$ in the definition of $F_{\rm eff}$ is found from Equation (40), valid both for positive $F$ (source) and negative $F$ (sink).

5.3.1. *Moderate sink strength: gravitational restoration and surface breaking*
The weak sinks considered above do not cause dramatic behaviour of the free surface. There is an almost uniform average depression, being modulated by an outgoing wave-train. Nonlinearity promotes these waves and also reduces the slope of the depression front as it propagates into undisturbed fluid. From low to moderate Froude numbers, we observe a relevant gravitational bounce back: the initial downward motion of the surface above the sink is reversed and the surface moves upwards, eventually attaining a stationary value. This bounce-back gravitational restoration is physically very elementary, just like filling in a crater of missing fluid. In Figure 19 we see a very weak bounce back above the sink appearing already at $F = -0{\cdot}2$. The gravitational restoration increases in importance as we increase the sink strength until $F \simeq -0{\cdot}6$. From then on it fades out, and exists no more at $F = -0{\cdot}7$.

When there is no gravitational restoration, one would expect the free surface to collapse toward the sink. This is what happens at infinite depth, [10, 11]. This tendency is apparent in Figure 20 where solutions due to increasingly stronger sinks are superimposed at time instants for which surface breaking appears. The horizontal extent of the displaced portion of the free surface sharply diminishes as the sink strength increases, while the vertical penetration is more than doubled passing from $F = -0{\cdot}4$ to $F = -0{\cdot}8$. The surface starts to break at $-F = 0{\cdot}4$, after a gravitational time about 4·3 (*cf.* Figure 19). Then there is breaking after shorter and shorter time until $F = -0{\cdot}8$. Figure 21 shows the latest evolution of surface breaking for

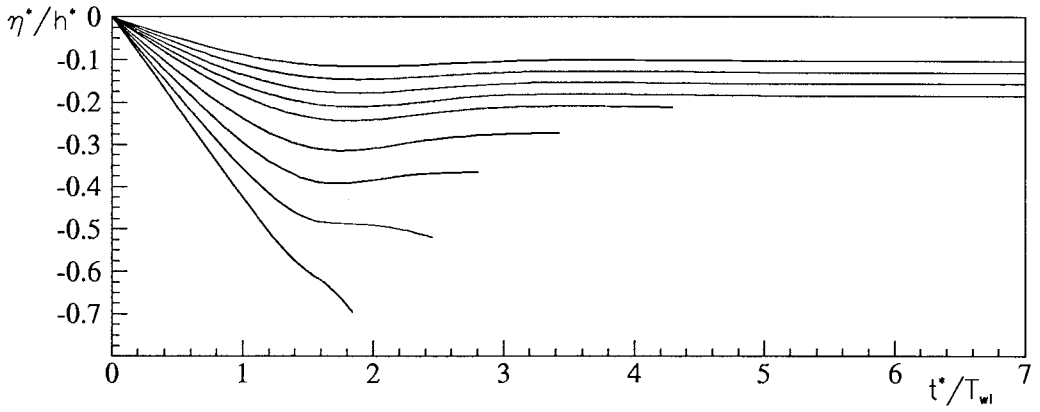


*Figure 19.* Time evolution of the Lagrangian point above the sink ($x^\star/h^\star = 0$) for $F = -0{\cdot}2$, $-0{\cdot}25$, $-0{\cdot}3$, $-0{\cdot}35$, $-0{\cdot}4$, $-0{\cdot}5$, $-0{\cdot}6$, $-0{\cdot}7$, $-0{\cdot}8$. For $|F| \geq 0{\cdot}35$, the numerical simulation is stopped because of breaking.

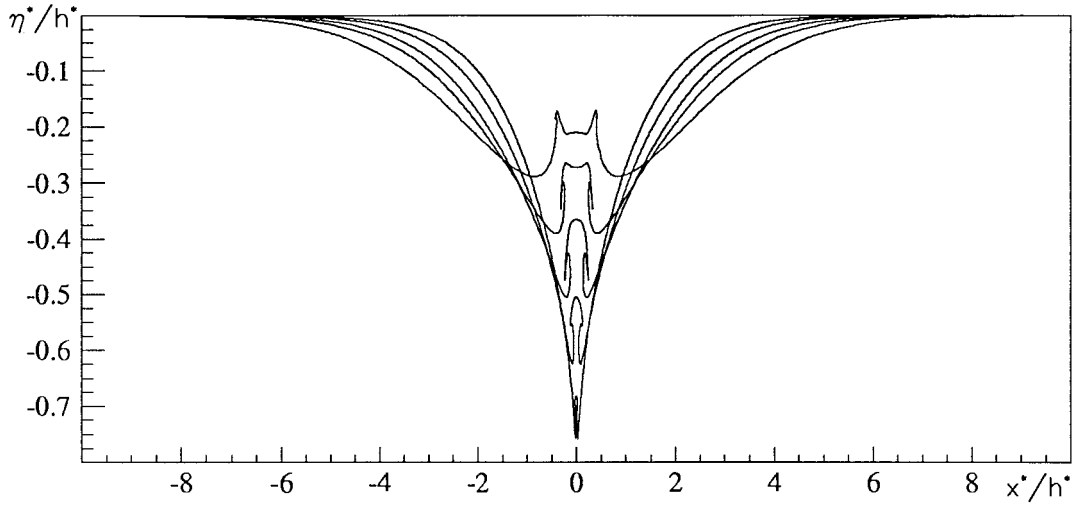


*Figure 20.* Free-surface profiles for $F = -0{\cdot}4$, $-0{\cdot}5$, $-0{\cdot}6$, $-0{\cdot}7$, $-0{\cdot}8$ for time $t = 4{\cdot}299$, $3{\cdot}423$, $2{\cdot}882$, $2{\cdot}296$ and $1{\cdot}806$, respectively.

$F$ ranging from $-0{\cdot}4$ to $-0{\cdot}7$. Geometrical details are sensitive with respect to increasing Froude number, the main feature being the reduction of the horizontal separation between the two breakers. A notable feature for $F = -0{\cdot}7$ is the tendency of the positive and negative branches of the free surface to reconcile, almost to isolate the breaking bulge of fluid. The high curvature of the free surface would probably imply a significant role of surface tension effects, presently not modeled. The gravity is still able to produce a tiny jet for $F = -0{\cdot}8$, while for $F = -0{\cdot}9$ computations predict a continuous collapse of the free surface toward the bottom sink.

5.3.2. *Dip instability above a strong sink*

The dip instability is a gravitational collapse of the free surface into the sink. It is a familiar phenomenon in a bath-tub, often accompanied by a vortex. The first scientific investigation of the dip instability in a tank drained from the bottom was done by Lubin and Springer [25]. They performed experiments and presented a simplified analysis for dip instability based on

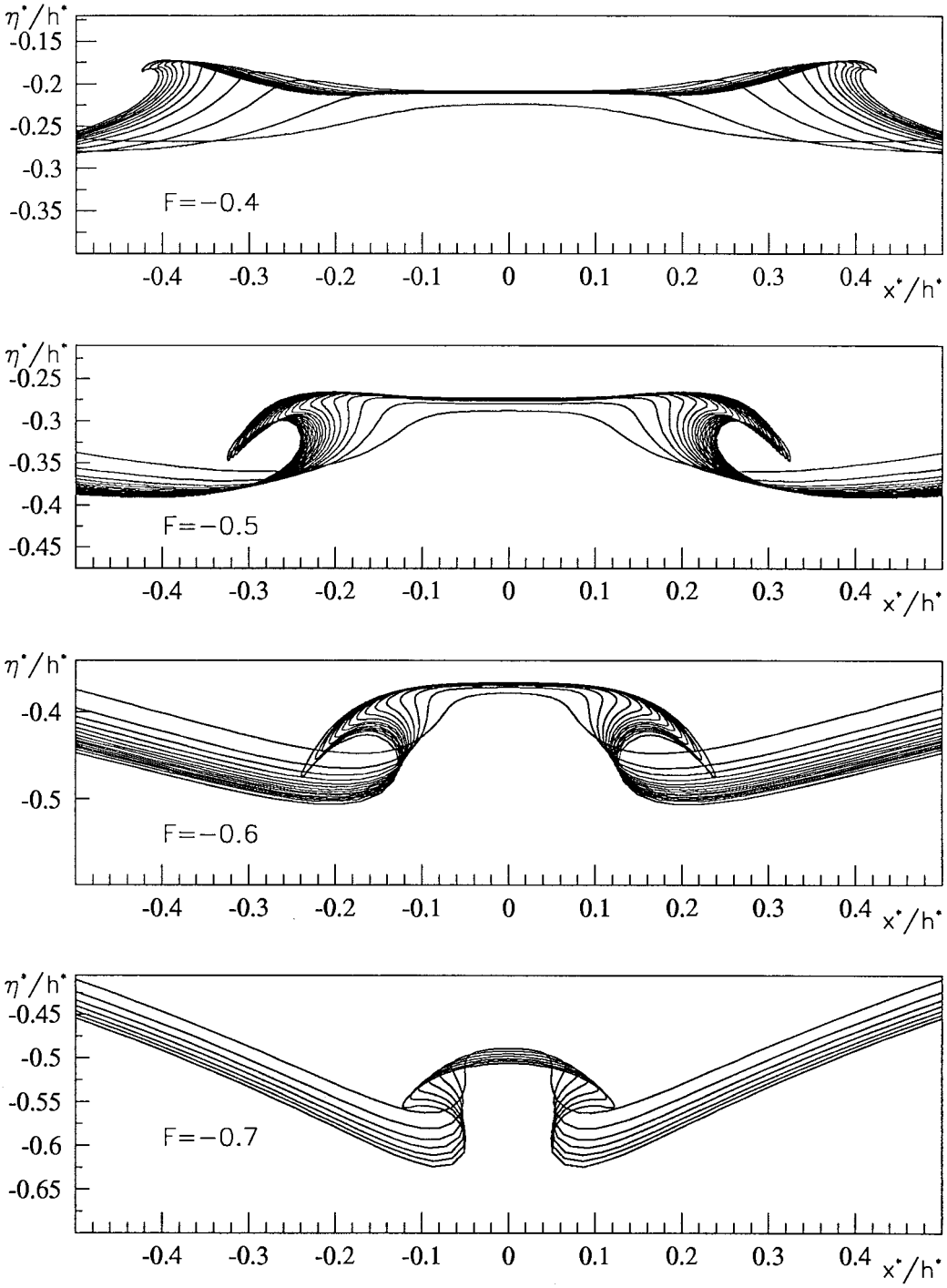


*Figure 21.* Enlarged view of the free-surface evolution above the sink for $F = -0{\cdot}4, -0{\cdot}5, -0{\cdot}6, -0{\cdot}7$.

Bernoulli's equation. In [26], Zhou and Graebel investigated dip formation numerically for an axisymmetric container, drained impulsively through a hole in the bottom. Tyvand [8] presented a simple analytical model leading to dip formation: the submerged line sink parallel to a free surface. The resulting impulsive flow was calculated to third order in a small-time expansion. A critical Froude number $\hat{F}_c = -1/3$ was found, representing the change of sign of the third-order elevation above the sink. The similar problem for a submerged point sink has been solved by Miloh and Tyvand in [10], where they found a critical Froude number $\hat{F}_c = -0{\cdot}2582$. These critical Froude numbers were taken as criteria for dip formation: there would be an early acceleration of the surface into the sink if the $\hat{F} < \hat{F}_c$. However, Xue and Yue [11] demonstrated numerically that this critical Froude number based on the third-order balance between nonlinearity and gravitational rebound could only be considered as a lower bound. In fact, they solved the fully nonlinear axisymmetric problem and found that dip instability takes place for all $\hat{F} < -0{\cdot}1930$. In [9], Kim performed a numerical study of the two-dimensional submerged sink, in agreement with [8].

The usual definition of the Froude number for these earlier sink papers is:

$$\hat{F} = \frac{Q^\star}{2\pi\sqrt{g^\star h^{\star 3}}} = \frac{1}{2\pi} F \ .$$

This is valid in two dimensions, where the source strength $Q^\star/(2\pi)$ is preferred instead of its flux. In three dimensions the source strength is given by the flux divided by $4\pi$. We will now derive the analytical criterion for dip formation based on the third-order analysis for an impulsive bottom sink in two dimensions.

The third-order elevation above a sink consists of the three terms given in Equation (30), with sign changes everywhere because the source is replaced by a sink. We will evaluate these three terms just above the sink $x = 0$. First we have the term independent of gravity which is given by the second-order potential:

$$\eta_{3,\infty}(0) = -\frac{1}{3}\left(\frac{k}{\pi}\right)^3 \sum_{\text{n odd}} \sum_{\text{m odd}} \sum_{\text{q odd}} \operatorname{sech} k_n \operatorname{sech} k_m \operatorname{sech} k_q \times$$

$$\times \left[ k_{n-m} k_{n-m-q} \tanh k_{n-m} \tanh k_{n-m-q} + k_{n-m} k_{n-m+q} \tanh k_{n-m} \tanh k_{n-m+q} + \right.$$

$$\left. + k_{n+m} k_{n+m-q} \tanh k_{n+m} \tanh k_{n+m-q} + k_{n+m} k_{n+m+q} \tanh k_{n+m} \tanh k_{n+m+q} \right]$$

We are interested in the limit $L \longrightarrow \infty$ and $L = 50$ should give a good approximation, especially at $x = 0$ where the influence from the artificial neighboring sinks is the smallest. We have chosen $L = 50$ with each of the triple series truncated after $N = 1001$. The result with 12 digits is: $\eta_{3,\infty}(0) = -0{\cdot}10280837928$ which is equal to: $\eta_{3,\infty}(0) = -\pi^2/96$ within an accuracy of nine nonzero digits.

The contribution from the lower-order potentials is: $\eta_{3\,\eta_1}(0) = \pi^2/192 = 0{\cdot}05140418959$ Numerically, we have now found a very simple relationship: $\eta_{3,\infty}(0)/\eta_{3\,\eta_1}(0) = -2$ . The gravity-dependent third-order elevation above the sink is:

$$\eta_{3,F} = \frac{1}{3F^2}\frac{k}{\pi} \sum_{\text{n odd}} k_n \tanh k_n \operatorname{sech} k_n \ . \tag{41}$$

We search for the limit as $L \longrightarrow \infty$. A computation using MATHEMATICA for the case after $L = 50$ gives the result when several thousand terms are included in the series: $F^2\eta_{3,F}(0) =$

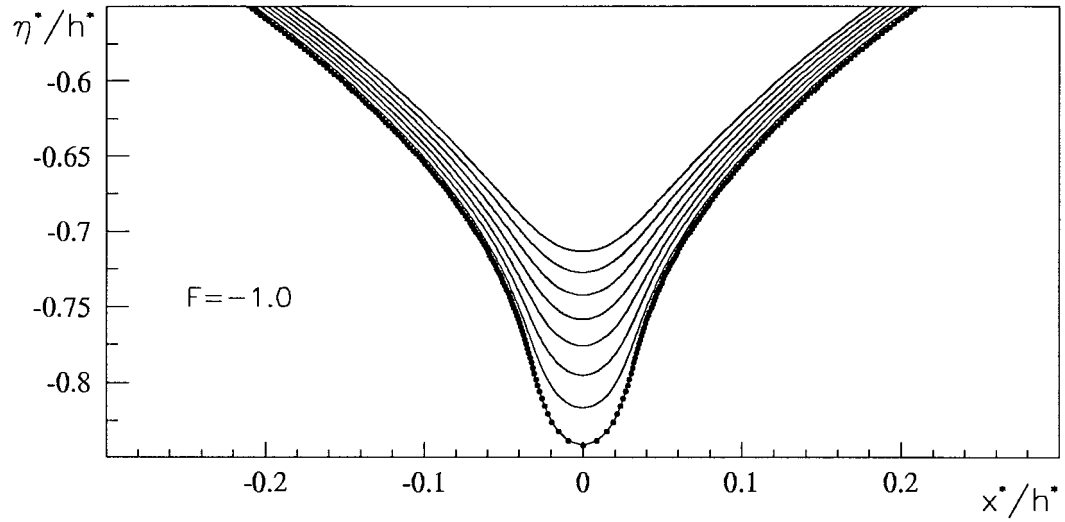


*Figure 22.* Late evolution of the dip forced by a constant sink. Enlarged view in natural scale for $t^\star/T_{\rm lw} = 1{\cdot}1, \ldots, 1{\cdot}17$ (0·01).

1/12. This result remains exactly the same for all $L$ between 26 and 55, with six nonzero digits accuracy. But it starts to diverge for larger $L$, due to roundoff errors. When $L < 26$, the period length is short enough to influence the result. The total third-order surface elevation above the impulsively-started bottom sink is: $\eta_3(0) = [F^{-2} - \pi^2/16]/12$ . A critical Froude number $F_{\rm c}$ is defined by the third-order elevation equal to zero, $\eta_3(0) = 0$, and this gives the result:

$$F_{\rm c} = -\frac{4}{\pi} \simeq -1{\cdot}2732395 \ . \tag{42}$$

With the same Froude-number definition as [8, 9], we have $\hat{F}_{\rm c} = -2/\pi^2 \simeq -0{\cdot}20264237$, which is quite far above the value $-1/3$ for a submerged two-dimensional sink. This is reasonable because the bottom sink generates a much more concentrated free-surface flow.

As anticipated, this analytical result has to be considered a lower bound, because dip formation is numerically observed at least for $F < -0{\cdot}9$. Actually, in the range $-0{\cdot}8 < F < -0{\cdot}35$ computations have to be stopped because of surface breaking and it is not possible to determine the evolution on a longer time scale, so physical dip formation could happen even for weaker sinks.

In principle (see [24] for a recent discussion) a steady cusp-flow sink is possible for $F \leq -1$. In the present computations this is not actually observed. As an example, Koerber and Forbes [24, Table 1] give a cusp height of 0·247 for $F = -1$. In our computations the height is 0·158 for $t^\star/T_{\rm lw} = 1{\cdot}17$ (*cf.* Figure 22). Following a longer evolution would require a dynamic refinement because of the strong stretching of Lagrangian markers around the center of the dip. This has not been attempted, and we can only observe that the two branches of the free surface tend to join each other at a smaller depth. Therefore, it would be possible to have a steady cusped flow consistent with that computed in [24]. Anyway, other issues could be of concern: some of numerical nature (*e.g.* inhability of the present method to develop a singularity in the domain boundary), other related to the stability of such steady solutions (which, though existing, could not be reached through an unsteady evolution).

## 6. Conclusions

We studied some classes of nonlinear free-surface flows generated by bottom sources and sinks that are started impulsively. Two time scales are involved: first the early impulsive time scale up to $t \sim (h^\star/g^\star)^{1/2}$ since the start, where gravity is of secondary importance. Later on, the flow is governed by the gravitational time scale $(h^\star/g^\star)^{1/2}$.

A constant source may give rise to a progressive bore, where an increasing water level propagates into still water. We show that a seemingly undular bore shape will arise even in linear theory. But it is essentially a transient phenomenon. As time progresses, the undulations will spread and grow farther and farther away from the bore front. The characteristic, almost flat surface in the bulk of the bore is a nonlinear phenomenon. This becomes clear if we compare a steady source flow with a steady sink flow of moderate amplitude.

The sink will develop a propagating depression, which may look like a negative bore if the sink strength is very small. However, a sink of finite strength will develop and maintain a wave pattern within the depression, and its front will not grow steep as for a true bore generated by a source.

A clear explanation for the origin of the undulations in a weak bore seems to be lacking in the literature. We found that the undulations, most pronounced for bores with small amplitude, are gradually suppressed as the bore amplitude increases. We therefore link the bore undulations to those in the classical Cauchy-Poisson problem for a concentrated initial disturbance. Accordingly, we identify the characteristic wavelength of the undulations with the typical wavelength for the linearized Cauchy-Poisson problem. This is asymptotically given by an Airy function, with the length scale of the same order as the undisturbed fluid depth. One may ask if a fully linearized bore exists. It does, to a certain extent, as far as the picking of the typical undulation wavelength and the undulation frequency is concerned. But the steepening of the bore front and the spatial decay of the undulations going into the bulk of the bore are dominated by nonlinear effects. There is no steady solution of a Cauchy-Poisson problem for a concentrated disturbance. Accordingly, there cannot be any steady undular bore either. All bores will be time-dependent, with a time scale slower than the oscillation period for a particle in the waves as they passed by.

We consider a one-parameter family of bores, governed solely by their Froude number, which is the source flux made dimensionless in terms of gravitational units. Each bore has its unique time evolution. Bore breaking is investigated, and the transition between non-breaking and breaking bores takes place for a Froude number slightly smaller than one. The lowest bore height giving breaking is found to be 40% higher than the undisturbed water level. The details of bore breaking are sensitive with respect to the Froude number.

All the considered bores are essentially time-dependent. Undular (non-breaking) bores have been followed up to $t^\star/T_{\mathrm{lw}} \sim 200$. At that time a (small) positive growth rate of the leading crest is still observed. For breaking (undular- or not) bores, simulations were stopped. In both cases, viscous effects could be eventually relevant in determining the steady regime features [7].

A sink with Froude number of order one or greater, will lead to dip formation, which is a gravitational collapse where the free surface is swallowed into the sink. An analytical estimate for dip formation is given which, on the ground of our numerical results, results to be an upper bound for the actual sink strength required to induce the gravitational collapse.

A phenomenon exclusive for finite depth is that sinks somewhat too weak for dip formation will cause surface breaking. This is due to the lack of dispersion of the peak of upward

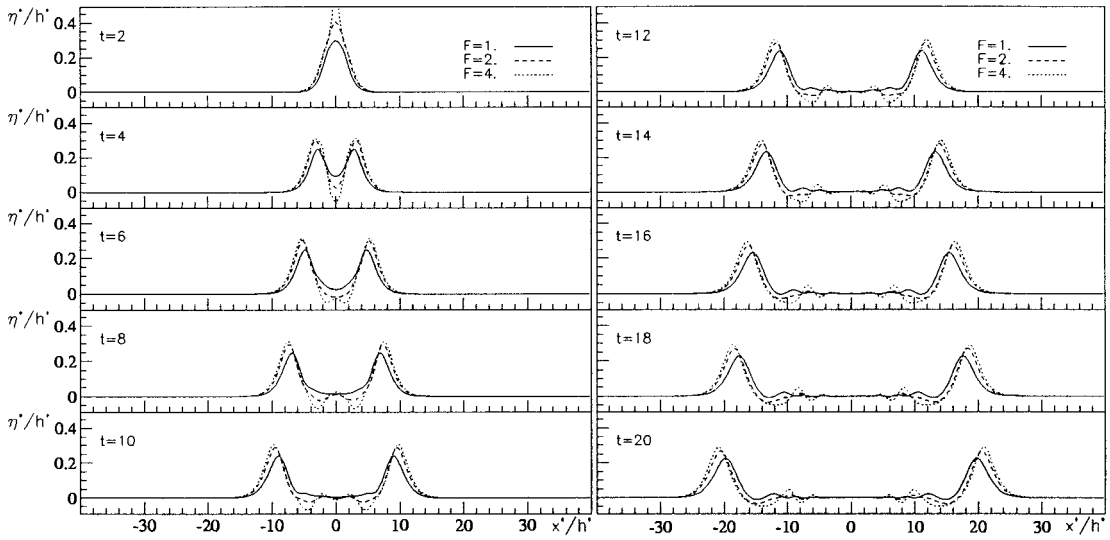


*Figure 23.* Disintegration of the initial hump due to a decaying source, $\sigma = 0{\cdot}5$. Time evolution of the free surface; non-dimensional $t = t^\star / T_{\mathrm{lw}}$ increases from top down and from left to right.

flow from the gravitational rebound. The horizontal extent of the breaking hump inside the depressed region shrinks gradually, leaving before disappearing a tiny upward jet [27] as the last attempt of the gravity to react to dip formation.

Impulsive sources decaying with time, $\sigma > 0$, have also been considered. A brief example is given in Figure 23, where the raised hump of water disintegrates into a leading solitary wave plus a train of dispersive waves. This behaviour is consistent with that observed for a conventional Cauchy-Poisson problem, where a free surface with finite amplitude is released from rest.

The long-time evolution of the wave system, *e.g.* the number of solitary waves, depends on the total mass of fluid emitted by the source, $1/\sigma$. This is shown in Figure 24, where wave patterns due to stronger sources are compared for $t^\star / T_{\mathrm{lw}} = 200$ ($F/\sigma^\star \sim 1/\sigma$, for $g/h^\star$ fixed). For $F = 0{\cdot}5$, a solitary wave is well separated from its dispersive tail. When $F$ is increased, the leading solitary wave is steeper and faster. In the last case, $F = 1{\cdot}75$, the injected mass is large enough to give rise to a second solitary wave of smaller amplitude. Further increasing $\sigma$ leads to breaking of the first emitted hump.

**Acknowledgements**

The research activity of M.L. is supported by the Italian *Ministero dei Trasporti e della Navigazione* through INSEAN Research Program 2000-2002. This work has been partly developed while the first author was visiting researcher at UCSB-OEL. The kind support of ONR, Dr. Ed Rood Program Manager, is gratefully acknowledged.

## Appendix A. Formulation for a dipole

The second basic type of singularity is the horizontal dipole located at the bottom. It represents the dominating far-field contribution due to a mass-conserving geological fault. The dipole

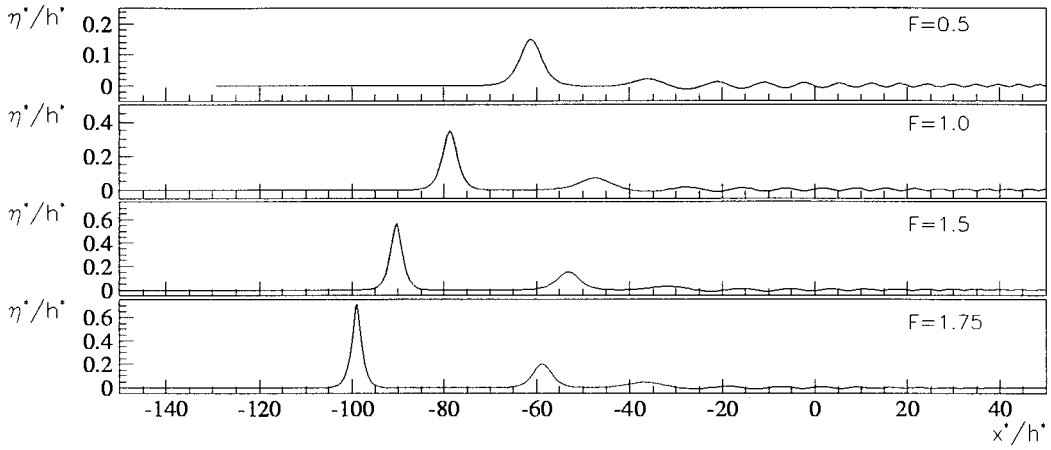


*Figure 24.* Long time behaviour of fluid packet for $F = 0{\cdot}5, 1, 1{\cdot}5, 1{\cdot}75$ and $\sigma^\star = 0{\cdot}25$. All wave profiles refer to $t^\star/T_{\mathrm{lw}} = 200$. The origin, $x = 0$, is the original location of the source.

strength is $\mu^\star$ and we accordingly redefine the Froude number as:

$$F = \frac{\mu^\star}{\sqrt{g^\star h^{\star 5}}} \tag{A1}$$

and the units of dimensionless velocity, time and pressure as $\mu^\star/h^{\star 2}$, $h^{\star 3}/\mu^\star$ and $\rho^\star\mu^{\star 2}/h^{\star 4}$, respectively. The bottom dipole is assumed to decay exponentially in time as $\mu^\star \mathrm{e}^{-\sigma^\star t^\star}$, with the dimensionless decay rate defined as:

$$\sigma = \frac{\sigma^\star h^{\star 3}}{\mu^\star} \ . \tag{A2}$$

So the dimensionless dipole strength is $\mathrm{e}^{-\sigma t}$. The integrated dipole strength does not have the same clear physical meaning as in the source case. The dimensionless unexpanded singular dipole potential is given by:

$$\psi = \frac{e^{-\sigma t}}{\pi} \sum_{-\infty}^{\infty} (-1)^n \frac{x}{x^2 + (y + 2n - 1)^2} \ . \tag{A3}$$

### A.1. First-order elevation

By taking minus the $x$-derivative of the expression for a bottom source, we find the first-order elevation for a bottom dipole:

$$\eta_1 = \frac{\pi}{4} \ \mathrm{sech}\left(\frac{\pi}{2}x\right) \ \tanh\left(\frac{\pi}{2}x\right) \ . \tag{A4}$$

The first-order elevation with artificial periodicity is now:

$$\eta_1 \ = \ 2\frac{k}{\pi} \sum_{\mathrm{n\ odd}} k_n \ \mathrm{sech}\ k_n \ \ \sin(k_n x) \ . \tag{A5}$$

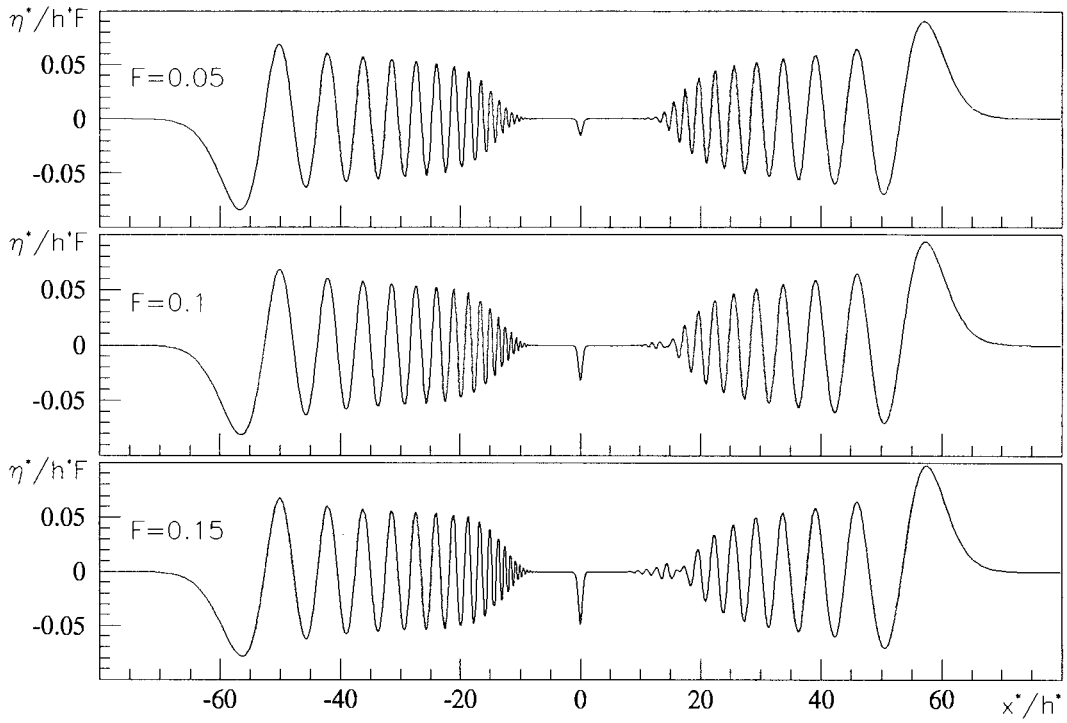


*Figure 25.* Free surface profiles due to a steady doublet for $t^\star/T_{\rm lw} = 60$. The strength of the doublet increases from top-down.

## A.2. SECOND-ORDER ELEVATION

In the dipole case, the periodic regular first-order potential at the free surface $y = 0$ is given by:

$$\varphi_1 \;=\; -\left(\frac{k}{\pi}\right)^2 \sum_{\rm n\ odd} \sum_{\rm m\ odd} k_n\, k_m \,\mathrm{sech}\, k_n \,\mathrm{sech}\, k_m [\cos(k_{n-m}x) - \cos(k_{n+m}x)] \tag{A6}$$

and the resulting second-order elevation by:

$$\begin{aligned} \eta_2 \;=\; & -\frac{1}{2}\left(\frac{k}{\pi}\right)^2 \sum_{\rm n\ odd} \sum_{\rm m\ odd} k_n\, k_m \,\mathrm{sech}\, k_n \,\mathrm{sech}\, k_m \;\times \\ & \times\, [\, k_{n-m} \tanh k_{n-m} \cos(k_{n-m}x) - k_{n+m} \tanh k_{n+m} \cos(k_{n+m}x)\,] - \\ & -\frac{\sigma}{8}\pi \;\mathrm{sech}\left(\frac{\pi}{2}x\right) \;\tanh\left(\frac{\pi}{2}x\right) \end{aligned} \tag{A7}$$

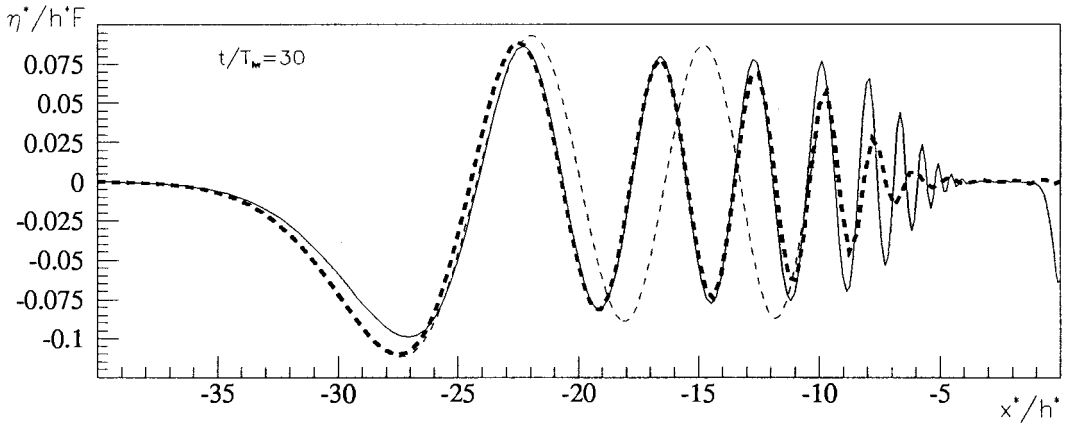


*Figure 26.* Leading wave system generated by a constant doublet. Comparison between fully nonlinear (solid line, $F = 0{\cdot}2$), linear (thick dashed line) and asymptotic solution (thin dashed line) of Equation (A10).

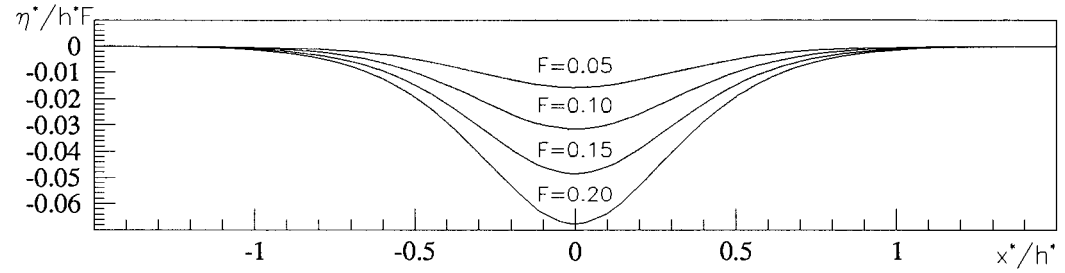


*Figure 27.* Enlarged view of the free surface about a constant doublet, $t^{\star}/T_{\mathrm{lw}} = 60$.

## A.3. THIRD-ORDER ELEVATION

The regular second-order potential at the free surface is:

$$\begin{aligned}\varphi_2 \;=\; & \left(\frac{k}{\pi}\right)^3 \sum_{\mathrm{n\ odd}} \sum_{\mathrm{m\ odd}} \sum_{\mathrm{q\ odd}} k_n k_m k_q \operatorname{sech} k_n \operatorname{sech} k_m \operatorname{sech} k_q \times \\ & \times \left\{ k_{n-m} \tanh k_{n-m} [\sin(k_{n-m+q}x) - \sin(k_{n-m-q}x)] + \right. \\ & \left. + k_{n+m} \tanh k_{n+m} [\sin(k_{n+m-q}x) - \sin(k_{n+m+q}x)] \right\} \\ & + 2\sigma \left(\frac{k}{\pi}\right)^2 \sum_{\mathrm{n\ odd}} \sum_{\mathrm{m\ odd}} k_n k_m \operatorname{sech} k_n \operatorname{sech} k_m [\cos(k_{n-m}x) - \cos(k_{n+m}x)] - \\ & - \frac{1}{F^2} \frac{k}{\pi} \sum_{\mathrm{n\ odd}} k_n \operatorname{sech} k_n \sin(k_n x) \;. \end{aligned} \tag{A8}$$

The third-order elevation is:

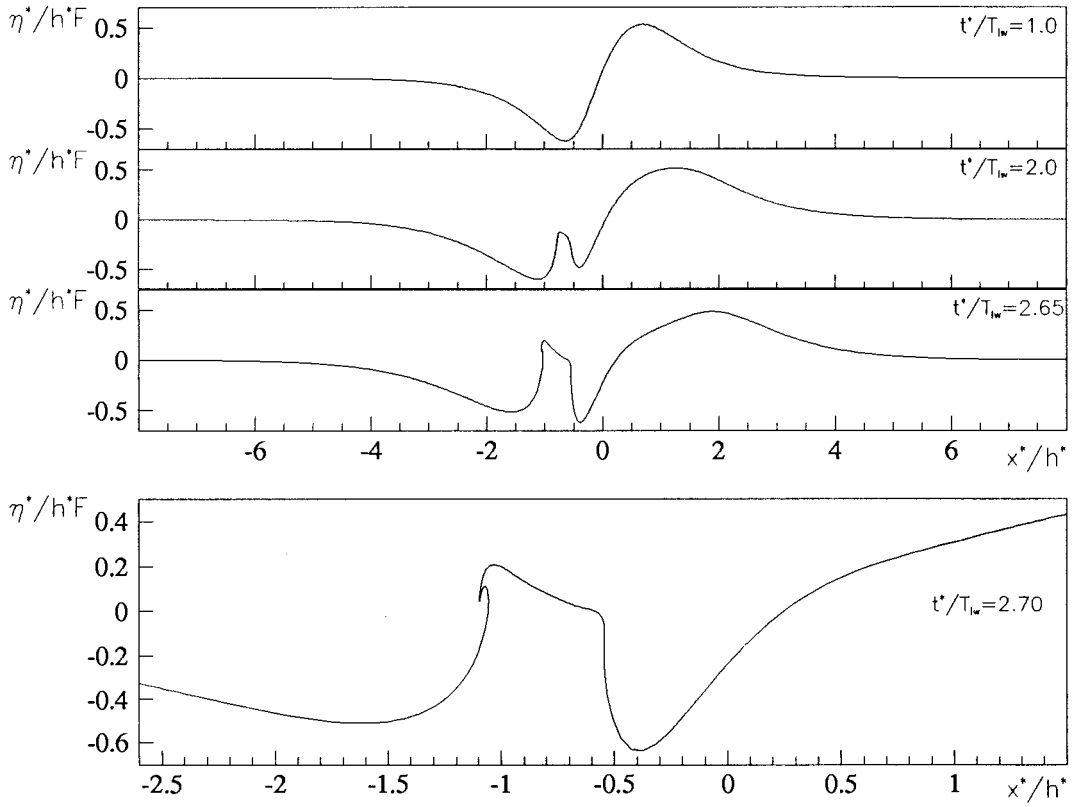


*Figure 28.* Free surface due to a steady doublet ($F = 0{\cdot}25$). The evolution stops with the clear evidence of surface breaking (see enlarged view in the bottom plot).

$$
\begin{aligned}
\eta_3 \;=\; & \frac{1}{3}\left(\frac{k}{\pi}\right)^3 \sum_{\text{n odd}} \sum_{\text{m odd}} \sum_{\text{q odd}} k_n k_m k_q \operatorname{sech} k_n \operatorname{sech} k_m \operatorname{sech} k_q \times \\
& \times \{\, k_{n-m} \tanh k_{n-m} [k_{n-m+q} \tanh k_{n-m+q} \sin(k_{n-m+q} x) - \\
& \quad - k_{n-m-q} \tanh k_{n-m-q} \sin(k_{n-m-q} x)] + \\
& + k_{n+m} \tanh k_{n+m} [k_{n+m-q} \tanh k_{n+m-q} \sin(k_{n+m-q} x) - \\
& \quad - k_{n+m+q} \tanh k_{n+m+q} \sin(k_{n+m+q} x)] \,\} \\
& + \frac{2}{3}\sigma \left(\frac{k}{\pi}\right)^2 \sum_{\text{n odd}} \sum_{\text{m odd}} k_n k_m \operatorname{sech} k_n \operatorname{sech} k_m \times \\
& \times [k_{n-m} \tanh k_{n-m} \cos(k_{n-m} x) - k_{n+m} \tanh k_{n+m} \cos(k_{n+m} x)] - \\
& - \frac{1}{3F^2} \frac{k}{\pi} \sum_{\text{n odd}} k_n^2 \operatorname{sech} k_n \tanh k_n \sin(k_n x) \;+\; \frac{\sigma^2 \pi}{24} \operatorname{sech}\left(\frac{\pi}{2} x\right) \tanh\left(\frac{\pi}{2} x\right) + \\
& + \frac{\pi^5}{24576} \left(51 \sinh\left(3\frac{\pi}{2} x\right) \;-\; 3 \sinh\left(5\frac{\pi}{2} x\right) - \right. \\
& \left. - 170 \sinh\left(\frac{\pi}{2} x\right)\right) \operatorname{sech}\left(\frac{\pi}{2} x\right) \sinh^7\left(5\frac{\pi}{2} x\right) \;. \qquad \text{(A9)}
\end{aligned}
$$

Here we have avoided the artificial periodicity wherever an exact formula is available.

### A.4. SAMPLE RESULTS

In the following, we report a few computations concerning the free surface motion due to a constant doublet. Wave patterns after $t^\star/T_{\rm lw} = 60$ are shown in Figure 25 for increasing strength of the submerged singularity. A linear analysis would imply a perfect anti-symmetric solution: this qualitatively explains the positive and negative leading waves propagating on the right and on the left, respectively. Following the arguments used for the source, the asymptotic behaviour of the leading wave is given by:

$$\eta = -\frac{1}{2}\mathrm{sign}(x) F \int_0^t \mathrm{e}^{-\sigma t} \left(\frac{2}{t-\tau}\right)^{2/3} \mathrm{Ai}' \left[\left(\frac{2}{t-\tau}\right)^{1/3} (|x| + \tau - t)\right] \mathrm{d}\tau \qquad \text{(A10)}$$

and its comparison with nonlinear, linear computations is offered in Figure 26. The agreement between solutions is reasonably good and consistent with that observed for the source (*cf.* Figures 11, 17).

A closer look at Figure 25 reveals that anti-symmetry is violated, even for the smallest strength. In particular, the right-propagating wave-train is made by fewer and longer waves with respect to the left propagating one. These features recall those observed when wave systems induced by (weak) sources and sinks, respectively, are compared.

The free surface between the two wave systems eventually remains flat and the only signature of the doublet is an unchanging dip which is not predicted on the basis of a linear theory. In particular, for cases considered in Figure 27, this depression results to be symmetric, in spite of the non-symmetric character of the forcing bottom flux considered, and it is deeper the stronger the doublet is.

Last plots, Figure 28, show the initial development of the wave motion forced by a doublet that is slightly stronger. After the early formation of the couple hump-hollow, as soon as the left depression rises, a localized surface breaking is detected and prevents any further computations. Similar behaviour has been observed for stronger singularities.

## References


1. H. Lamb, *Hydrodynamics*. New York: Dover (1932) 738pp.
2. J.V. Wehausen and E.V. Laitone, Water waves. In: W. Flugge (ed.) *Handbuck der Physik* (Vol. 9). Berlin: Springer (1960) pp. 446–778.
3. G.B. Whitham, *Linear and Nonlinear Waves*. New York: J. Wiley (1974) 636pp.
4. C.C. Mei, *The Applied Dynamics of Ocean Surface Waves*. Singapore: World Scientific (1983) 740pp.
5. J.L. Hammack, A note on tsunamis: their generation and propagation in an ocean of uniform depth. *J. Fluid Mech.* 60 (1973) 769–799.
6. D.H. Peregrine, Calculations of the development of an undular bore, *J. Fluid Mech.* 25 (1966) 321–330.
7. A.F. Teles da Silva and D.H. Peregrine, Nonsteady computations of undular and breaking bores. In: *Proc. 22nd Int. Conf. Coastal Engng.*, Delft. A.S.C.E. 1 (1990) 1019–1032.
8. P.A. Tyvand, Unsteady free-surface flow due to a line source *Phys. Fluids* A4 (1992) 671–676.
9. M.J. Kim, Numerical study of dip formation using sink array model. *Int. J. Modern Phys.* C8 (1997) 1249–1262.
10. T. Miloh and P.A. Tyvand, Non-linear transient free-surface flow and dip formation due to a point sink. *Phys. Fluids* A5 (1993) 1368–1375.
11. M. Xue and D.K.P. Yue, Nonlinear free-surface flow due to an impulsively-started submerged point sink. *J. Fluid Mech.* 364 (1998) 325–347.

12. D.H. Peregrine, Flow due to a vertical plate moving in a channel. Unpublished note (1972).
13. M. Greenhow and W.-M. Lin, Nonlinear free surface effects: experiments and theory. Report 83-19. MIT, Dept. of Ocean Engineering (1983).
14. P.A. Tyvand and A.R.F. Storhaug, Green functions for impulsive free-surface flows due to bottom deflections in two-dimensional topographies. *Phys. Fluids* 12 (2000), 2819–2833.
15. P.A. Tyvand and M. Landrini, Free-surface flow of a fluid body with an inner circular cylinder in impulsive motion. *J. Eng. Math.* (2000) to appear.
16. P. Bassanini, C.M. Casciola, M.R. Lancia and R. Piva, A boundary integral formulation for kinetic field in aerodynamics. Part I: Mathematical analysis. Part II: Applications to unsteady 2D flows. *Eur. J. Mech. B/Fluids* 10 (1991) 605–627 and 11 (1992) 69–92.
17. A. Sidi and M. Israeli, Quadrature methods for periodic singular and weakly singular Fredholm integral equations. *J. Sci. Comp.* 3 (1988) 201–231.
18. P. Sonneveld, CGS, A fast Lanczos-type solver for nonsymmetric linear systems. *SIAM J. Sci. Stat. Comp.* 10 (1989) 36–52.
19. G. Graziani and M. Landrini, Application of multipoles expansion technique to two-dimensional nonlinear free surface flows. *J. Ship Res.* 43 (1999) 1–13.
20. M.S. Longuet-Higgins and E.D. Cokelet, The deformation of steep surface waves on water. I A numerical method of computation. *Proc. R. Soc. London* A 350 (1976) 1–26.
21. J.W. Dold, An efficient surface integral algorithm applied to unsteady gravity waves. *J. Comp. Phys.* 103 (1992) 90–115.
22. M. Abramowitz and I.A. Stegun, *Handbook of Mathematical Functions*. New York: Dover (1965) 1046pp.
23. T.B. Benjamin and M.J. Lighthill, On cnoidal waves and bores. *Proc. R. Soc. London* A224 (1954) 448–460.
24. A.J. Koerber and L.K. Forbes, Cusp flows due to an extended sink in two dimensions. *J. Eng. Math.* 36 (1999) 349–360.
25. B.T. Lubin and G.S. Springer, The formation of a dip on the surface of a liquid draining from a tank. *J. Fluid Mech.* 29 (1967) 385–390.
26. Q.-N. Zhou and W.P. Graebel, Axisymmetric draining of a cylindrical tank with a free surface. *J. Fluid Mech.* 221 (1990) 511–532.
27. M.S. Longuet-Higgins and H.N. Oguz, Critical jets in surface waves and collapsing cavities. *Phil. Trans. R. Soc. London* A 355 (1997) 625–639.